Electrical, Photoluminescence and Optical Investigation of ZnO Nanoparticles Sintered at Different Temperatures

Ahmed Sedky (✉ sedky196000@hotmail.com)
Assiut University

Atif Ali
King Khlad University

H.H Somaily
King Khlad University

H Algarni
King Khalad University

Electrical, Photoluminescence and Optical Investigation of ZnO Nanoparticles Sintered at Different Temperatures

A.Sedky[1*], Atif Mossad Ali[2], H.H. Somaily[2] and H. Algarni[2]

[1]Physics Department, Faculty of Science, Assiut University, Assiut, Egypt
[2]Physics Department, Faculty of Science, King Khalid University, Abha, Saudi Arabia

Abstract

We report here structural, electrical, photoluminescence (PL), and optical investigations of ZnO nanoparticles. The ZnO samples are initially sintered at various temperatures (T_s) (600-1200 °C) temperatures and their size is reduced twice to nanoscale by using ball friction at 200 rpm rotational speed and 30 minutes duration. It is found that the T_s do not influence the well-known peaks associated with the ZnO hexagonal structure, whereas the constants of the lattice and the average crystallite diameters are affected. Although the nonlinear area is observed for all samples in the I-V curves, the breakdown field E_B and nonlinear coefficient β are moved to lower values as T_s increases, while the residual voltage K_r and nonlinear conductivity (σ_2) are increased. The empirical relations for K_r, E_B, and β as a function of T_s are; $K_r = 0.004\ T_s – 0.487$, $E_B = -1.786 T_s +2559.5$ and $\beta = -0.052\ T_s +75.19$. On the other hand, a maximum UV absorption shift (A_{max}) is obtained at 412 nm, 400 nm, 384 nm, and 326 nm as the T_s increases up to 1200 °C. For each sample, two different energy band gap values are obtained; the first is called the basic bandgap (E_{gh}) and its value above 3 eV, while the second is called the optical band gap (E_{gL}), and its value below 2.1 eV. Moreover, the empirical relations of them are $E_{gh} = 0.002\ T_s - 0.24$, $E_{gl} = -0.0033\ T_s +5.242$ and $\Delta E = -0.0015\ T_s +5.002$. Furthermore, the values of (N/m^*) and lattice dielectric constant ε_L are increased by increasing T_s up to 1200 °C, while the vice is versa for the interatomic distance R. The dielectric loss $\tan \delta$ is almost linear above 4 eV for all samples, and it decreases sharply as the T_s increases. The optical and electrical conductivities σ_{opt} and σ_{ele} are decreased as the T_s increases up to 1200 °C. Finally, the characteristic of UV band edges against the optimum value of PL intensity for the samples shows 8-continuous peaks. Furthermore, the PL intensity of the peaks is decreased by increasing T_s and also by shifting the UV wave number towards the IR region.

Introduction

 N-type ZnO with a large optical energy gap (3.3eV) and high Urbach energy (60-100 meV) was used early as a varistor to avoid the high voltage overloads [1-2]. ZnO exhibits a nonlinear electrical conductivity of n-type through its twice-fold ionizations as a result of excess Zn ions. The excess of Zn ions gives origin to intrinsic donors in ZnO and can be assigned either as Frenkel defects to the interstitial Zn or as Schottky defects to the oxygen vacancy [3–7]. However, these intrinsic defects regulate the electrical conductivity of ZnO as oxygen vacancies, which originally formed below the conductive band at high temperatures during sintering, and were also known as donor defects [8-9]. Such defects tend to migrate to and annihilate the grain boundaries during the quenching cycle. The cycle of migration is usually slow and is triggered thermally near the grain boundaries and effectively eliminated [10]. It is generally accepted that the localized band gap states deplete the ZnO carriers on either side of the grain boundaries and generally lead to the creation of double Schottky barriers that govern the ZnO electrical properties [11-13].

Although in many applications ZnO has a wide range, there is a lack of data based on its thermal stability, particularly when ZnO samples sintered at high temperatures [18, 19-23]. Different models such as the ion migration model and model of defects have investigated the heat treatment, which affect electrical stability in ZnO. They suggested that Zn interstitials may be formed in the depletion layer during sintering and frozen by either quenching or slow cooling to room temperature [24-25]. It is also accepted that some of these defects could be formed at the grain boundary, such as donor-like positive charge and acceptor as negative charge, affecting the ZnO properties [26-27]. In addition, some of the positive Zn charges (Zn^+ and Zn^{++}) may also be formed in the depletion layer, but these ions can be extracted by thermal annealing [28]. Although much of the work has been done on the effect of sintering temperature on the non-linear I-V characteristics of ZnO varistors, there are few investigations have been carried out on optical constants investigations. It is accepted that the evaluation of optical constants of ZnO has significant importance in optoelectronic and optical applications such as filters, modulators, solar cells, photodiode, switches, etc. [29-32]. Therefore, it is necessary to get some information on its optical absorption, especially when sintered at different temperatures. This will help us for more investigation on the energy of localized states, bandgap energy, and free carriers determination through UV absorption analysis. On the other hand, photoluminescence (PL) at room temperature usually provides additional insight into the crystal nature of semiconducting materials through emission from discrete expansion of the state and within bandgap or structural defect states. In a wide gap of ZnO semiconductor, the UV-blue PL emission band is often narrowed, and usually represents a radiative process near band edge (NBE). The NBE emission can be delineated as a photo-excitation of charging carriers from valance band to conductive band resulting in the formation of exciton (electron-hole pair) and subsequent radiative recombination of electrons and holes. Reducing the nano-particle size also constitutes an effective method for the properties of ZnO [33-37]. For example, when the ZnO is prepared in nanoscale dimensions, the transition temperatures (T_C) from semiconducting to metallic state are effectively changed. Furthermore, some of the optical properties, such as dielectric constant, electrical, and optical conductivities, are improved [38-39]. However, further research still needed in order to take advantage of this potentially high stability of ZnO ceramic for satisfying overload voltage requirements.

To explain the connection between sintering temperature, which typically reflects intrinsic defects, and ZnO properties, structural, electrical, and optical properties of sintering temperature are well investigated in the range of (600-1200 °C). Furthermore, we are trying to improve the performance of ZnO by reducing the grain size to the order of nanoscale. Moreover, a detailed investigation of the electrical and optical constants against sintering temperature is introduced. Anyhow, by increasing sintering up to 1200°C, we could increase lattice dielectric constant, residual voltage, optical energy gap, and nonlinear electrical conductivity. While the fundamental energy gap, electrical and optical conductivities, and dielectric loss factors are decreased. On the other hand, the characteristic of UV band edges against the optimum value of PL intensity for sintered ZnO nanoparticles shows 8-continuous peaks. Furthermore, the PL intensity of the peaks is decreased by increasing sintering temperature and by shifting the UV wave number towards the IR region. However, these results gave us more hooping for ZnO stability optimization during the sintering process.

Experimental Details

The 10 g of ZnO powder (Aldrich 99.999% purity) is thoroughly mixed in the correct proportions and calcinated in box furnace at 1000 °C in air for 16 hours. The resulting powders are ground, divided into four equal parts and pressed into 4 pellets and then sintered separately for 16 h in air at different temperatures of 600, 800, 1000, and 1200 °C. Finally, the samples are quenched in the air down to room temperature. After that, the size of each sample is reduced to the order of nanoscale by using a mechanical ball milling machine at 200 rpm rotational speed and 30 minutes cycle time. To avoid the temperature impact, this process is repeated twice for fine nanoparticles. The sample phase purity is examined using x-ray diffraction pattern (Philips PW-1700) with wavelength Cu-Kα radiation at 40 KV and 30 mA settings, and at a diffraction angle range (20°-70°) with a step of 0.06°. A high-resolution electron microscope (HRTEM) (JEM-100-CXII plus JEOL microscope working at 120 kV) is used to examine sample morphology on a nanoscale. With Keithley electrometer, 5kVdc power supply and digital multimeter, I-V characteristics at RT (2 mm thick and 10 mm diameter) are obtained. The samples between two copper electrodes are well polished and sandwiched, and the current is measured proportional to the voltage applied. The optical properties at room temperature was measured against wavelength (200–1000 nm) using a JascoV-570 (Japan) computer programmable double beam with UV–visible–NIR spectrophotometer at standard incidence with a scan speed of 1000 mm min^{-1}. (Photometric accuracy of ±0.002–0.004 absorbance and ± 0.3% transmittance). In the case of reflectivity measurement, an additional attachment model ISN-470 is provided. A supplementary attachment model ISN-470 is given in the case of reflectivity measurement. Finally, spectra of emission of photoluminescence in the room temperature are measured using a spectro-fluorometer JASCO FP-6300.

Results and Discussions

The theoretical ρ_{th} of the samples is calculated from XRD analysis by using the relation, $\rho_{th} = \dfrac{nW}{N_A V}$, where n is the number of atoms per unit cell ($n = 2$ for ZnO), N_A is Avogadro's number, W is the molecular atomic weight of the composition and V is the volume of unit cell ($V = a^2 c \sin 60$). The ρ_{th} listed in Table 1 is slightly decreased by increasing sintering temperature T_s form 4.733 to 4.682 (g/cm^3). These values are between (81% - 81.89 %) of theoretical density 5.78 g/cm^3 for ZnO [40]. X-ray

diffraction patterns shown in Figure 1 can be identified as the hexagonal wurtzite structure with space group P63mc, [ICDD card no: 04-008-8198]. Although no additional peaks are formed for all samples, the average value of the peaks intensity listed in Table 1 is increased from 1931.3 to 2298.8 as the T_s increases up to 1200 °C. The lattice parameters a and c listed in Table 1 are between (3.243-3.255 Å) for a-parameter, and between (5.196 - 5.218 Å) for c- parameter, in agreement with the previous data based on ZnO [42-45]. The increase of lattice parameters by increasing T_s can be attributed to the change of the crystallite size and lattice strain due to thermal expansion induced by temperature, which is completely approved in the next paragraph. To support our data for increasing the lattice constants by T_s, ZnO nanoparticles can be transferred to microscale by annealing above 400 °C.

However, the ZnO wurtzite structure usually deviates from the ideal arrangement by changing the u-parameter, which describes the length of the bond parallel to the c-axis. The values of the u-parameter, calculated by $U = 0.333(\frac{a}{c})^2 + 0.25$ [46], are listed in Table 1. U-parameter is nearly constant (u ~ 0.379) for all T_s values. This indicates that the four tetrahedral distances stay almost constant through a distortion of tetrahedral angles due to the long-range of polar interactions [47-48]. The Zn-O bond length (L) is calculated using $L = [(\frac{a^2}{2}) + (0.5 - U)^2 c^2]^{\frac{1}{2}}$ [49]. The values of L are between 2.376Å and 2.385 Å for all T_s values. This behavior is consistent with the reported data based on ZnO [50-52].
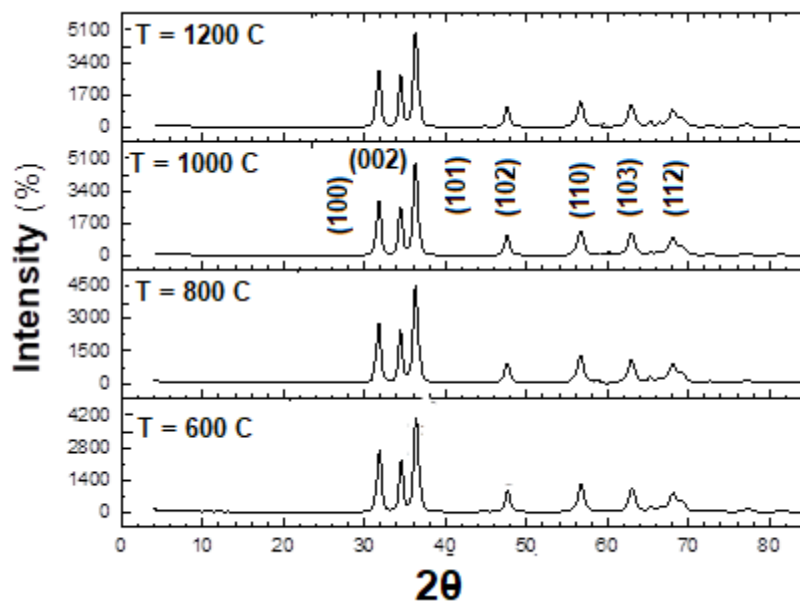

Figure 1: X-ray diffraction pattern for ZnO nanoparticles.

The average crystallite size D_{hkl} is determined by using the Lorentz square method, in terms of X-ray line broadening, according to the following Scherer's formula [53-56];

$$D_{hkl} = \frac{k\lambda}{\Delta\theta \cos\theta} \tag{1}$$

where λ is the wavelength (λ = 1.5418 Å) of X-ray, $\Delta\theta$ is the half-maximum line width, θ is the Bragg angle, and k is a constant (K = 0.9 for ZnO). D_{hkl} values given in Table 1 are 21.89, 22.53, 23.29, and 24.70 nm for T_s values. Although the grain sizes are in the same order of magnitude, D_{hkl} is increased as T_s increases. The dislocation density (δ) is calculated in terms of D using $\delta = 1/D^2$ formula [57-58]. The lower values of δ listed in Table 1 (0.0016 - 0.0021) indicate that ZnO nanoparticles have very few lattice defects and good crystalline qualities. The TEM graphs shown in Fig. 2 indicated that the nanoscale morphology for ZnO nanoparticles is in the order less than 100 nm. This is in good agreement with XRD line broadening size calculations.

Table 1: Density, lattice parameters, c/a and u values, the intensity of the peaks, average crystallite diameter, dislocation density, and Zn-O bond length versus T_s for ZnO nanoparticles.

T_s (C)	ρ (gm/cm^3)	a (Å)	c (Å)	c/a	V ((Å)^3)
600	4.733	3.243	5.196	1.601	47.325
800	4.704	3.251	5.206	1.601	47.651
1000	4.694	3.253	5.210	1.601	47.746
1200	4.682	3.255	5.218	1.601	47.878
T_s (C)	u	D (nm)	δ	L (Å)	I
600	0.3797	21.89	0.0021	2.376	1931.3
800	0.3798	22.53	0.0020	2.382	2045.8
1000	0.3798	23.29	0.0018	2.384	2143.7
1200	0.3796	24.70	0.0016	2.385	2298.8

T = 600 ºC   T = 800 ºC

T = 1000 ºC   T = 1200 ºC
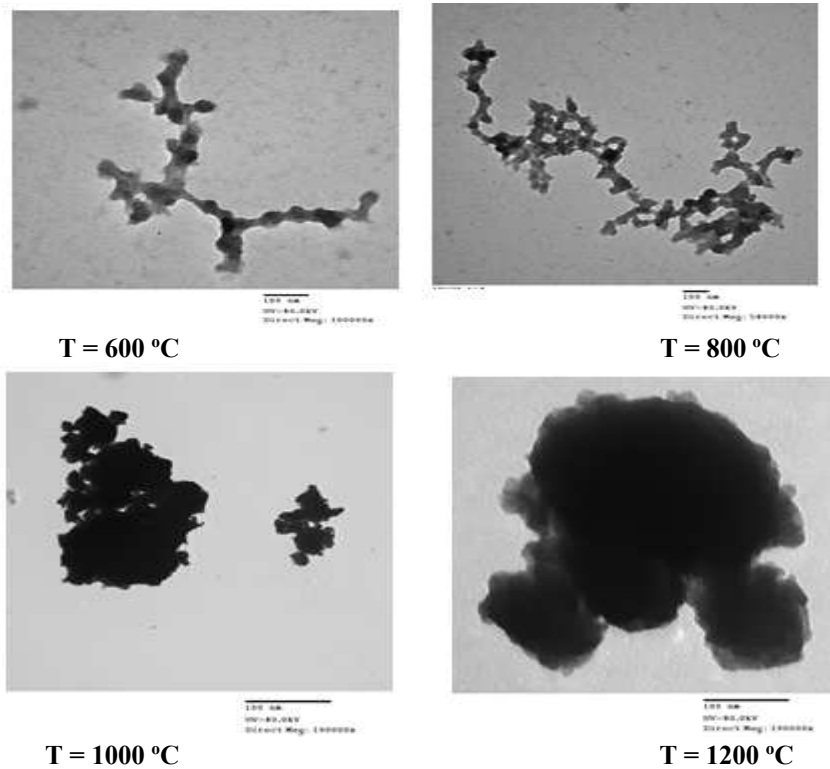
Figure 2: TEM images for ZnO nanoparticles.

3.2-I-V Characteristics

The I-V curve pattern shown in Figure 2 is linear in low and high field regions as well as nonlinear in the intermediate field region. The field is shifted to lower values with increasing Ts, whereas current density shifted to higher values. When the current flowing through the varistor is one mA / cm², the breakdown field EB is usually taken as the field applied. The EB values mentioned in Table 2 decrease from Ts= 600 °C at 1428.6 V/cm to 1250, 714.3 and 416.7 V/cm at Ts= 800, 100 and 1200 °C, respectively. The current-voltage relation of ZnO is given by the equation below [59-60];

$$J = (\frac{E}{C})^{\beta} \qquad (2)$$

Where J is the current density, E is the electric field being applied; C is constant, and β is the nonlinear coefficient. The slope of each curve gives the value of β in the upturn region [61] by plotting the current-voltage curves on a log-log scale; Table 2 lists the values of β as against Ts. For Ts= 800, 100 and 1200 oC, the β values are decreased from 42.27 at Ts= 600 oC to 37.12, 21.2, and 12.75, respectively. These results indicate that the increase in Ts to 1200 oC decreases non-ohmic characteristics and moves the breakdown fields to lower values. This is due to the decrease in the height of the potential barrier formed at the ZnO grain boundaries, which is usually caused by oxygen vacancies, in accordance with the data published [62, 63-66].
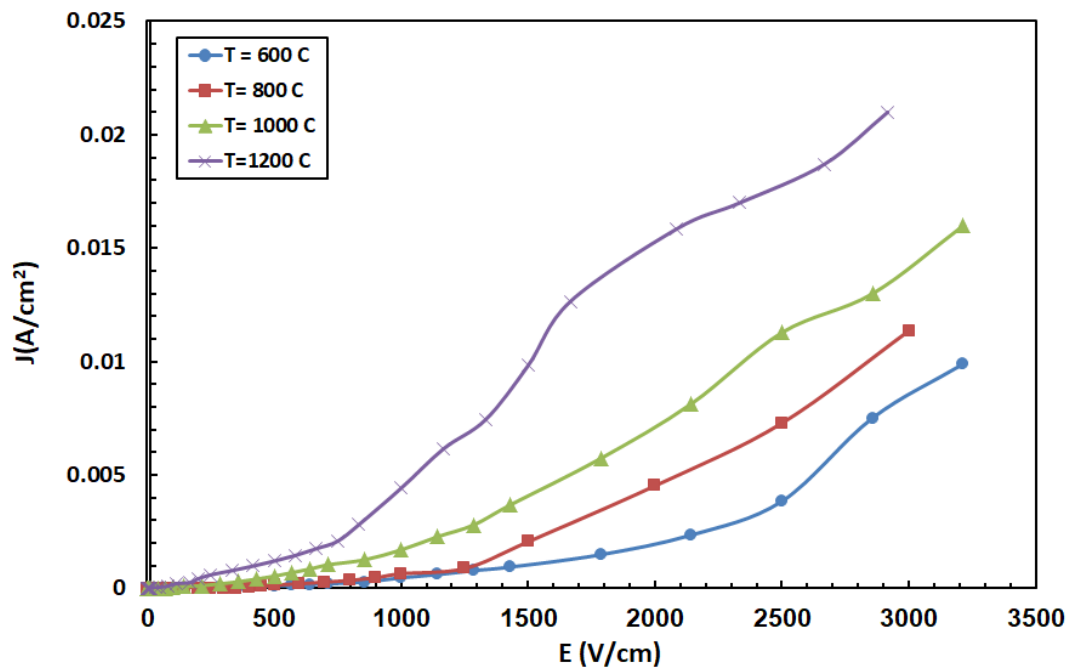

Figure 3: J-E curves versus T_s for ZnO nanoparticles.

ZnO varistor's residual voltage ratio K_r is defined as the ratio of the electric field to a given current impulse and the breakdown field E_B for a fixed diameter and ZnO thickness as follows; (7.4 mm < D < 21 mm), (0.5 mm <d < 4.5 mm). However the empirical formula for the ZnO varistor relationship between Kr and E_B is given by [67];

$$K_r = b_0 + \frac{b_1}{E_B} \qquad (3);$$

For pure ZnO, the values of b_0 and b1 are 1.21 and 1370 V/cm. However, the dimensions of the samples present are in the same range as those recorded (D = 10 mm, d = 2 mm) [67]. Therefore, the Kr values are found to be respectively 2.17, 2.31, 3.13, and 4.5. This is in good agreement with previous studies suggesting that low residual voltage ratio provides high nonlinearity coefficient β and breakdown field E_B, while high residual voltage ratio suggests low nonlinearity coefficient and E_B [67-68]. We determined the following empirical relationships, as seen in Figure 4, to clarify the consistency of the present work between $_{Kr}$, β, and E_B vs T_s. $K_r = 0.004\ T_s - 0.487$ $T_s = -1.786\ T_s + 2559.5$ and $\beta = -0.052\ T_s + 75.19$. This reveals a direct proportional to Ts for K_r, and an inverse proportional to E_B and β. In addition, $E_B = 0$ temperature is $T_s = 1433.09$ °C and $K_r = 5.732$ and $\beta = 0.669$. Furthermore, in the first ohmic region, we calculate the electrical conductivity σ_1 by using the Ohms law ($\sigma_1 = \Delta J/\Delta E$) [68] in the first ohmic region, and σ_2 in the upturn region by the following formula [68];

$$\sigma_2 = \sigma_1 \exp\{\frac{(\beta-1)(E_2 - E_1)}{E_2}\} \qquad (4);$$

where E_1 and E_2 are the fields which are extended around nonlinear area boundaries. Table 2 lists the values of E_1, E_2 σ_1, and σ_2 across the two regions. It is observed that the electrical conductivity for the nonlinear and breakdown fields is gradually increased by that T_s, in accordance with the obtained behavior.
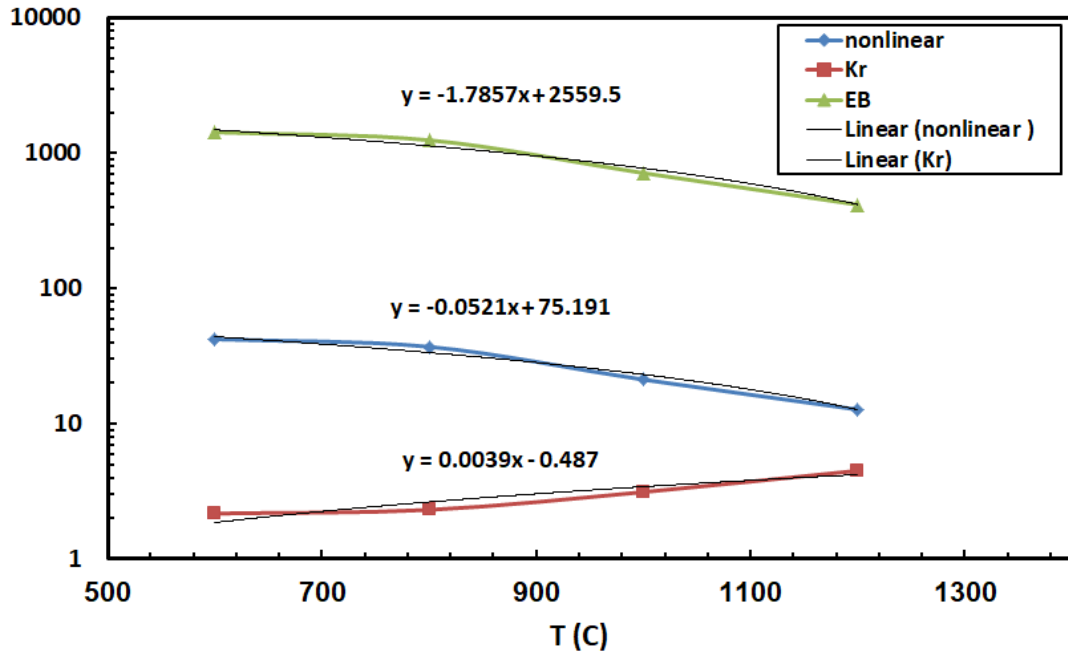

Figure 4: E_B, β and K_r versus T_s of ZnO nanoparticles.

Table 2: Breakdown field, nonlinear coefficient, residual voltage, and electrical conductivity versus T_s for ZnO nanoparticles.

T_s	E_B	β	K_r	σ_1	E_1	E_2	σ_2
(°C)	(V/cm)			$(\Omega.cm)^{-1}$	(V/cm)	(V/cm)	$(\Omega.cm)^{-1}$
600	1428.6	42.27	2.17	6.63E-14	21.43	28.57	1.99E-9
800	1250	37.12	2.31	5.78E-14	150	220	5.66E-9
1000	714.3	21.20	3.13	3.19E-12	2.85	7.14	5.95E-7
1200	416.7	12.75	4.50	3.61E-9	16.67	33.33	4.54E-4

3.3- Optical Measurements and Energy Gap

Figures 5(a,b) display the optical absorbance (A) and the optical reflectance (R) at the wavelength. There is a gradual increase in ZnO nanoparticles absorbance, with decreasing wavelength. There is also an increase in absorbance by increasing near-infrared photon energy area (exciton peaks ~ 300 nm) for all samples, which can be due to an increase in free carrier concentration as the photon energy increases.
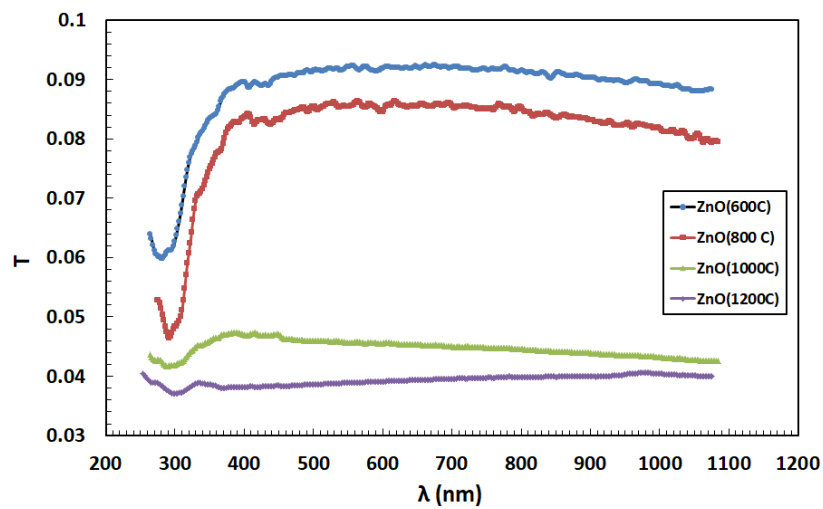

Figure 5(a): Transmittance versus wave length for ZnO nanoparticles
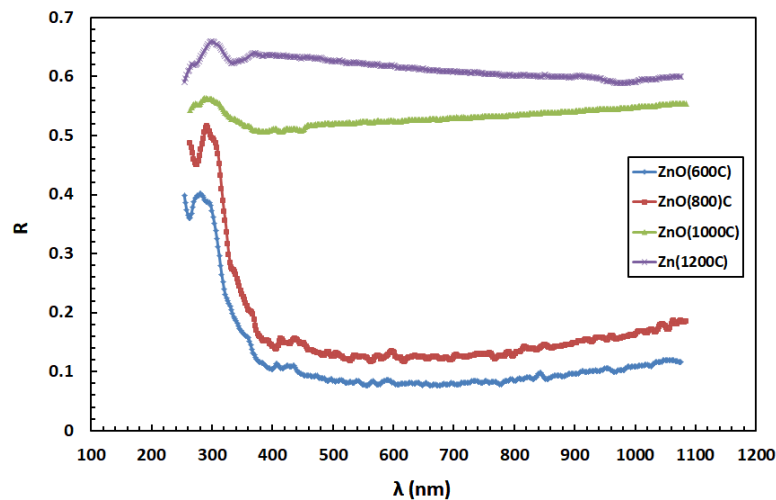
Figure 5(b): Reflectance versus wave length for ZnO nanoparticles

In addition, by rising T_s to 1200 °C, absorbance is reduced. This behavior may be related to oxygen vacancies, making ZnO highly suitable for oxygen sensor use [69]. The efficiency of the sensor depends on the reactions between ZnO oxide defects and atmospheric oxygen [70-71]. Reducing the absorption peaks by T_s may be related to increasing the particle size and also decreasing the band gap of ZnO as T_s increases.

Exciton energy can only be considered for materials with the larger Urbach energy like ZnO (100 meV), and is provided by photon energy (hc/α_{max}) against maximal absorption or lower reflection.The maximum (A_{max}) or minimum (R_{min}) value given in Table 3 is 412 nm (3.01 eV), 400 nm (3.10 eV), 384 nm (3.23 eV), 326 nm (3.81 eV), i.e. UV change. For optical band gap E_g determination the average value of absorption coefficient α is determined using the formula, $\alpha = 2.303 \ln (A/t)$ and $\alpha = (1-R^2/2R)$, where t is the distance traveled by the photons to the thickness solution, t = 12 mm. For optical band gap E_g determination, the average values of absorption coefficients α are determined using the formula, $\alpha = 2.303 (A/t)$, where t is the distance traveled by the photons to the thickness solution, t = 8.5 mm. After that, E_g is calculated using the following Tauc equation [72]:

$$(\alpha \upsilon)^{\frac{1}{m}} = A(h\upsilon - E_g) \qquad (5)$$

A is constant, α is the coefficient of absorption, Lisboa is the frequency of photons, and h is the constant of Planck, respectively. M is a parameter that characterizes electronic transition form and takes 1/2 for direct transition permitted by ZnO. Therefore, E_g is calculated by extrapolating to $\alpha = 0$ [73-74] the linear portion of the plot of $(\alpha h \upsilon)^2$ versus the photon energy $h\upsilon$ to $\alpha = 0$ [73-76]. From Fig. 6(a) for ZnO, it can be observed that α values increase as photon energy increases, and it is significantly affected by T_s increase up to 1200 °C where the edge of absorption also shifted to higher power Anyhow, from the plot shown in Fig, two different energy gap values are apparent. 6(a). At higher photon energy (UV region), the first bandgap (E_{gh}) is obtained, while the second one (E_{gl}) is obtained at lower photon energy (visible area). For ZnO nanoparticles the action of E_g against T_s is shown in Figure 6(b), and related values are summarized in Table 2. For ZnO nanoparticles the values of E_{gh} and E_{gl} are 4.07, 3.95, 3.5, 3.25 eV and 1.05, 1, 1.55, 2.1 eV respectively. This suggests a decline in E_{gh}, while E_{gl} is increased as the T_s rise to 1200 °C. Two optical energy gaps, however, are also recorded for semiconductors of the form n [77-80]. In principle, this can be interpreted as follows in terms of the conduction shape and valence bands. The electronic transition from the valence band (VB) top or bottom to the conductive band (CB) top or bottom, which is consistent with the higher absorption values (homo-lumo), could take place at higher photon energy and assuming the geometric symmetry. Nonetheless, when the phonon energy is reduced, the energy may not be adequate for the above transformation to take place. Thus, the transfer of the electron takes place only from the top of VB to the bottom of CB, which coincides with the lower values of the absorptions.
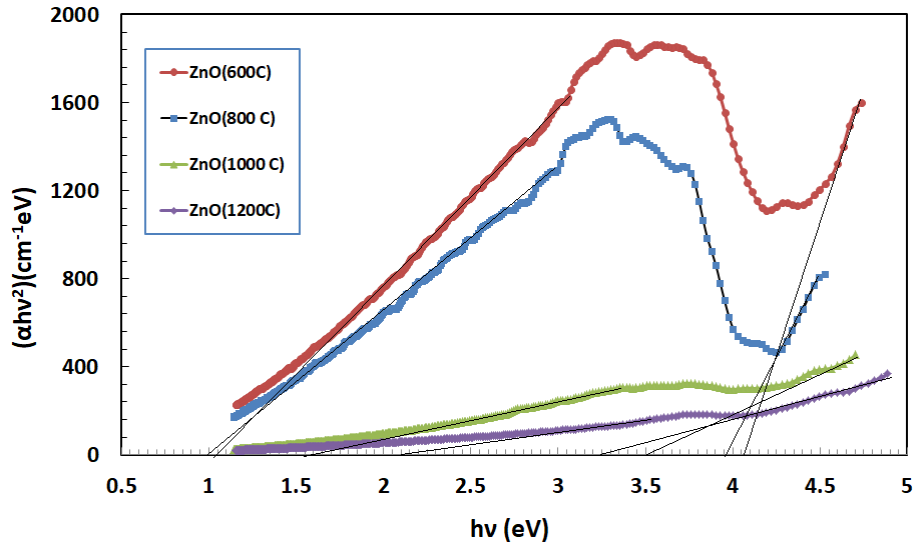
Figure 6(a): $(\alpha h v)^2$ versus photon energy for sintered ZnO nanoparticles.
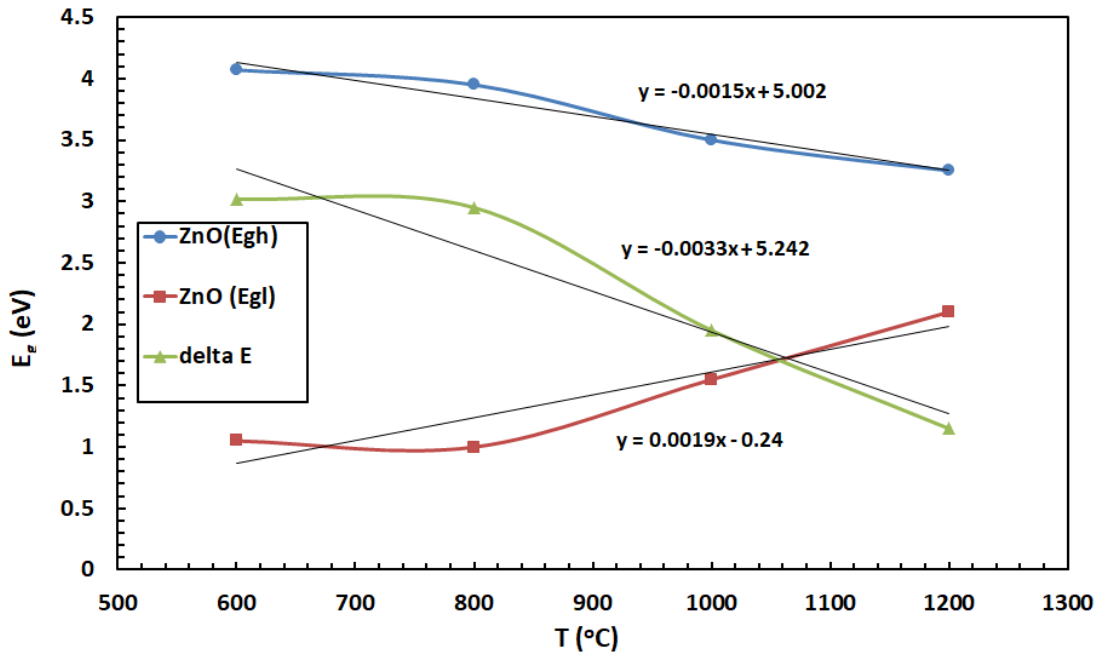
Figure 6(b): E_g versus T_s for ZnO nanoparticles.

Generally, this behavior is in good agreement with the reported data based on n-type semiconductors [81-82]. However, an exciton is a quasi-particle formed upon optical excitation of an electron from VB into CB. They thereby created charge vacancy in the VB; the positively charged hole induces an attractive Coulomb interaction toward the electron in CB. Hence, they can form a bound pair state, with a finite binding energy. Therefore, fluctuation of absorption close to shorter wave lengths may be due to either of the motion of electron-hole pairs as well as an electron or due to possible interference between reflected lines that occurs at high photon energy and affect electron transition from VB to CB. To support the above idea, the curvature occurs at high energy of photon and it is also higher at lower T_s (600 and 800 °C) and then decreased as T_s increases to 1200 °C. Consequently, fluctuation of absorption is inversely proportional with T_s in the present samples. Therefore, two different gaps are supposed to occur.

The crystalline and oxygen vacancies defects have significant effects on the optical band gap of ZnO. The ZnO is usually characterized by structure disorder and contains typically some defects which produce localized states [83-84]. These defects are higher for the ZnO sintered at 600 ℃, and consequently, E_{gh} is 4.07 eV, which is higher than E_{gh} for ZnO (3.2 eV). Additionally, the decrease of the optical band gap to 3.25 eV by increasing T_s up to 1200 ℃ may be due to increasing free carrier concentration as listed in Table 3, thereby resulting in a shortening of the bandgap, which is well-known as Burstein-Moss effect [85]. It is also evident from Table 3 that $\Delta E = E_{gh} - E_{gl} = 3.02, 2.95, 1.95$, and 1.15 eV for the ZnO nanoparticles, in which ΔE is decreased as the T_s increases as well as E_{gh} behaviors.

To clarify the consistent of the present work between E_{gh}, E_{gl}, and ΔE against T_s, we determined the following empirical relations, as seen in Figure 6 (b). E_{gh} (eV) = 0.002 T_s – 0.24, E_{gl} (eV) = -0.0033 T_s +5.242 and ΔE (eV) = -0.0015 T_s +5.002. This indicates direct proportional against T_s for E_{gh} as well as K_r and inverse proportional for ΔE and E_{gl} as E_B and β. Moreover, the temperature at which, $E_{gh} = 0$ is, $T_s = 120$ ℃, and in which $E_{gl} = 5.638$ eV and $\Delta E = 5.182$ eV.

3.4- Dielectric Constant and Optical Conductivity

The dielectric constant real part (ε_1) is determined by using the equation [86-87] ;

$$\varepsilon_1 = n^2 - k^2 = \varepsilon_L - \frac{e^2 N}{4\pi^2 \, \epsilon_\circ \, c^2 m^*} \lambda^2 \qquad (6a)$$

where e is the electronic charge, N is concentration of the free carriers, m* is effective mass, ϵ_o is permittivity of free space, c is light speed, and ε_L is residual lattice dielectric constant which represents high-frequency component of the relative permittivity at $\lambda = 0$. n is refractive index given from the values of reflectance R as follows;

$$n = \frac{1+R}{1-R} + (\frac{4R}{(1-R)^2} - K^2)^{\frac{1}{2}} \qquad (6b)$$

Figure 7 shows the behavior of (n^2-k^2) against λ^2 at different sintering temperatures for the samples.

Table 3: $\lambda(A_{max})$, E_c, E_{gH}, E_{gL}, N/m*, ε_L, of ZnO nanoparticles

| T (℃)	λ(nm) A_{max}	E_c (eV) A_{max}	E_{gH} (eV)	E_{gL} (eV)	ΔE (eV)
600	412	3.01	4.07	1.05	3.02
800	400	3.10	3.95	1.00	2.95
1000	384	3.23	3.50	1.55	1.95
1200	326	3.81	3.25	2.10	1.15
T (℃)	N/m* (g^{-1}cm^{-3})	N (cm^{-3})	R (cm)	slope	ε_L
600	2.4E+54	0.94E+30	8.98E-11	2E+7	1.21
800	4.92E+54	1.88E+30	7.13E-11	4E+7	1.48
1000	24.6E+54	9.40E+30	4.17E-11	2E+8	9.44
1200	49.2E+54	18.79E+30	3.31E-11	-4E+8	19.43
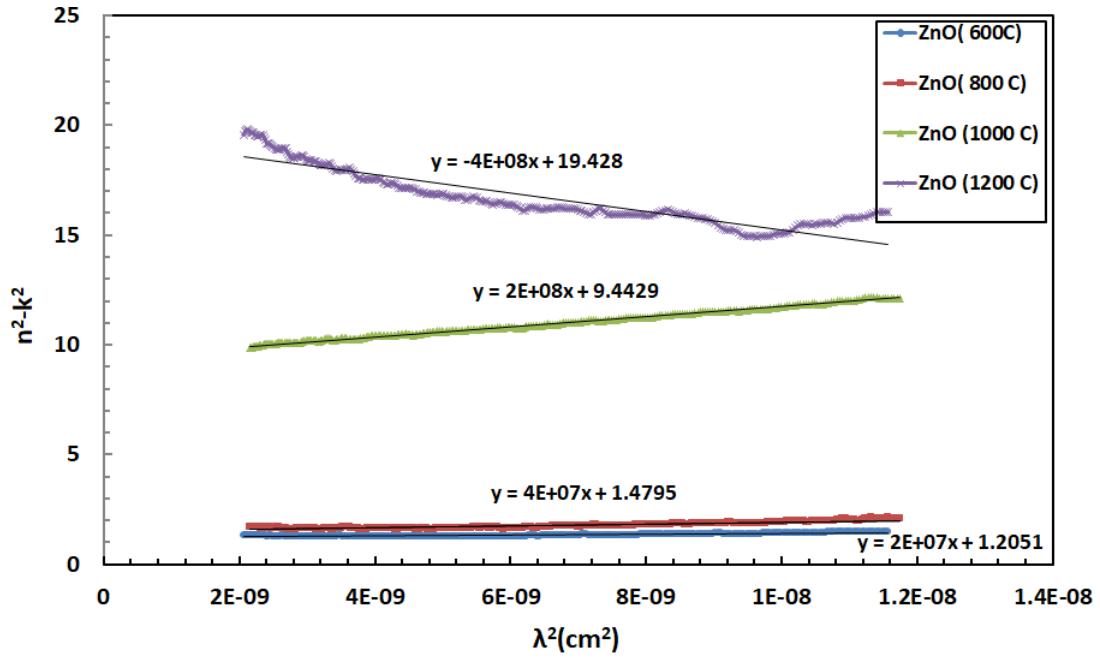
Figure 7: The relation between (n^2-k^2) and λ^2 for ZnO nanoparticles.

It is observed that this behavior is almost linear with a positive slope for ZnO nanoparticles sintered at T_s = 600 °C, 800 °C and 1000 °C, but it loses its linearity at the lower energy and the slope is changed to negative (-4E+8) for ZnO sintered at T_s = 1200 °C. N/m^* and ε_L are calculated from the slope of linear parts and extrapolation of the plot to $\lambda^2 = 0$, respectively. The values of (N/m^*) and ε_L for ZnO nanoparticles, listed in Table 2, are increased by T_s up to 1200 °C. A dramatic increase in the values of ε_L and (N/m^*) above 800 °C is also recorded. By looking at the present data, one can see that the optical energy gap, E_{gl}, (N/m^*), and ε_L seemed to be changed in the same manner. The increase of free carrier concentration up to T_s =1200 °C can be achieved by the decrease of oxygen deficiency or electrons in ZnO. For more clarification, free carrier concentration N is calculated using the average value of m^* which has been reported for ZnO (m^*=3.82× 10^{-25} g) [86], and therefore the inter-atomic distance (R) can be calculated by using the relation; R = (0.86/N $^{(1/3)}$) [66,67]. The values of N and R are listed in Table 2, and it is clear that N value is increased by increasing T_s, and the vice is versa for inter-atomic distance R.

The dielectric constant ε is a critical optical parameter because it usually provides information for the electronic structure of materials and helps for its design as optoelectronic devices. The dielectric constant is written as a function of the imaginary parts ε_1 and ε_2 as follows [89,90];

$$\varepsilon = \varepsilon_1 - i\varepsilon_2$$

$$\tan\delta = \frac{\varepsilon_2}{\varepsilon_1} = \frac{2nk}{n^2 - k^2} \qquad (7)$$

where tan δ is the dielectric loss factor generated from the constant dielectric components ε_2 and ε_1. These components are given in terms of extinction coefficient (k) and refractive index n. k is responsible for attenuation of light, and ε_1 is responsible for attenuation of the electrical field causing dielectric loss. The relation between tan δ and hν is shown in Figure 8. It is found that tan δ is almost linear above 4 eV at constant T_s and decreases sharply as the photon energy increases. Also, tan δ is decreased as the T_s increases, and the drop of tanδ at T_s = 1200 °C can be attributed

to the increase in polarization probability occurred by increasing temperature, in agreement with the reported data [91-92].
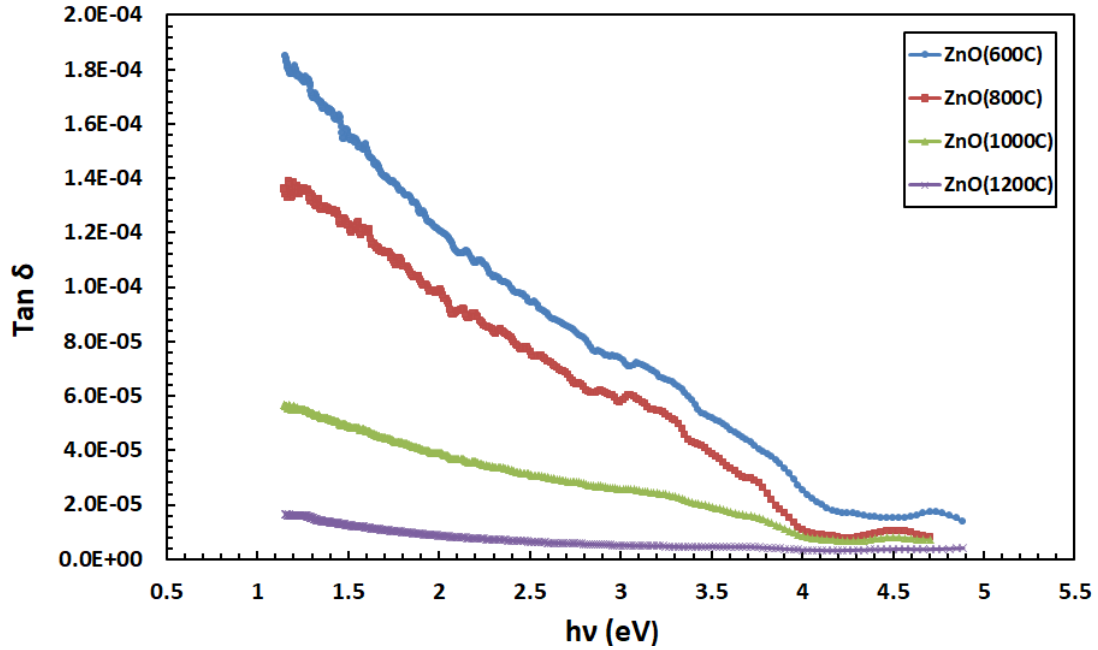

Figure 8: Dielectric loss versus hv for ZnO nanoparticles.

The optical response is mainly obtained for any material in terms of optical conductivity (σ_{opt}) which is determined using the following formula [93-94];

$$\sigma_{opt} = \frac{\alpha n c}{4\pi} \qquad (8a)$$

Also, the electrical conductivity (σ_{ele}) due optical response of the material is given by;

$$\sigma_{ele} = (\frac{2\lambda}{\alpha})\sigma_{opt} \qquad (8b)$$

The behavior of σ_{opt} and σ_{ele} against photon energy for ZnO nanoparticles is shown in Figure 9(a, b). Although the behavior of σ_{opt} is unsystematic against photon energy, it is generally decreased by increasing T_s. The behavior of σ_{ele} against photon energy is similar to dielectric loss, but it is gradually decreasing as the T_s increases up to 1200 ºC. However, the higher value of σ_{opt} as the photon energy increases assures the high photo-response of the sintered samples. This behavior is due to the increase of electron excitation by photon energy and sintering temperature [95-96]. It can also be noticed that σ_{ele} decreases as the photon energy increases, which confirms the metallic behavior [97].
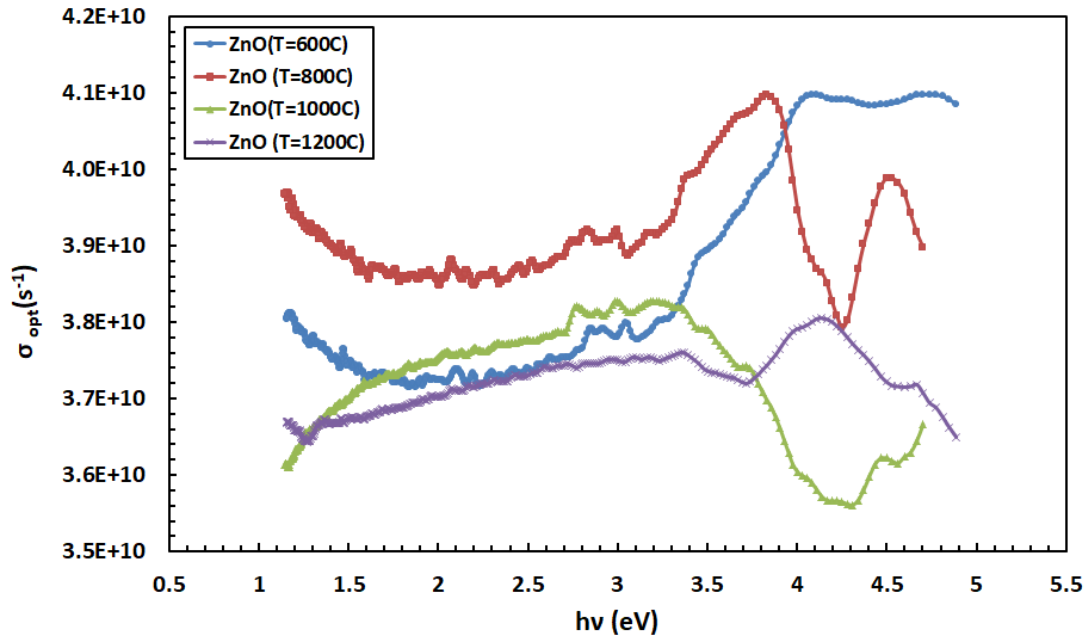
Figure 9 (a): Optical conductivity versus hv for ZnO nanoparticles.
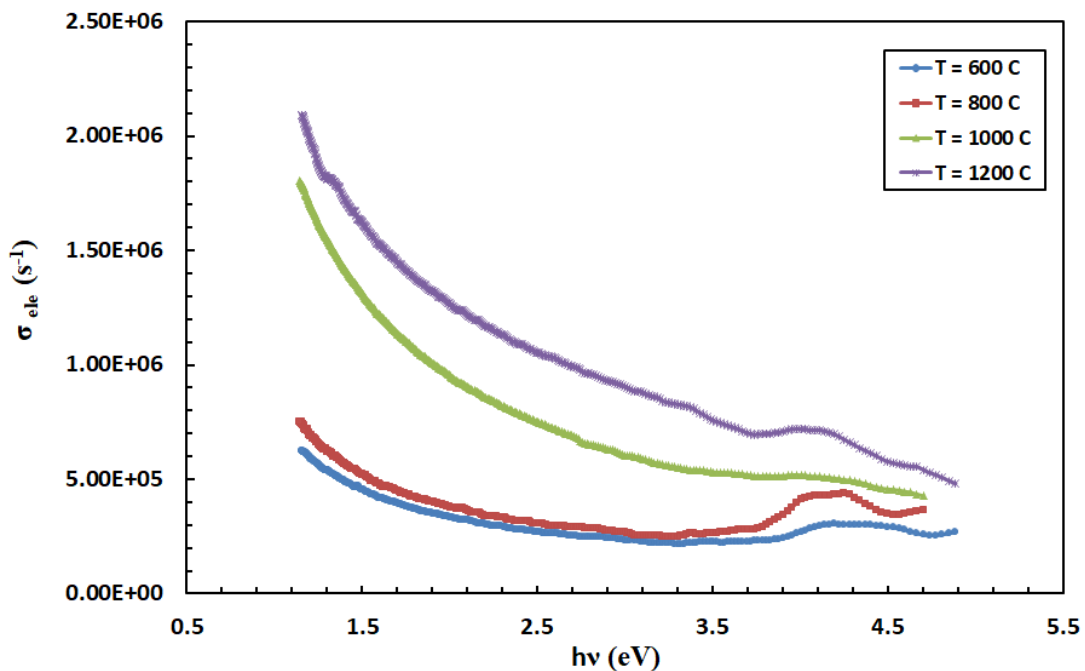
Figure 9 (b): Electrical conductivity versus hv for sintered ZnO nanoparticles.

3.5- photoluminescence (PL)

The characteristic of UV band edges against the optimum value of PL intensity for sintered ZnO nanoparticle is shown in Figure 10. However, eight continuous peaks could be recorded for ZnO nanoparticles, as listed in Table 4. Further, the PL intensity of the peaks is decreased by increasing T_s and also by shifting the wavenumber towards the IR region. Interestingly, the first and second peaks, which give strong UV emission are obtained at the range of (393 - 405 nm). These peaks agree very well with the reported ultraviolet energy-gap of bulk ZnO ~ 3.2 eV [97]. It is commonly considered that the band edge emission at ~400 nm should be attributed to the recombination of excitons from the localized level below the conduction band to the valance band [98]. In general, visible emission in ZnO is attributed to some of the

intrinsic defects such as oxygen vacancies V_o, zinc vacancies V_{Zn}, oxygen interstitials O_i, zinc interstitials Zn_i, and oxygen antisites O_{Zn}. The origin of indigo and violet emissions centered at the range of (409- 429 nm) (~ 2.90 eV) is related to electron transition from a shallow donor level of neutral Zn_i to the top level of the valence band [97]. This suggests that the shallow donor level of Zn_i is located at ~0.34 eV below the conduction band. Extra blue emissions centered at the range of (443- 477 nm) (~ 2.60 eV) and also bluish-green emission centered at (483- 486 nm) (~2.55 eV) are ascribed to radiative transition of an electron from the shallow donor level of Zn_i to an acceptor level of neutral V_{Zn} [100]. The green emission at the range of (500 -525 nm) (~2.35 eV) may be due to the donor-acceptor recombination or transition from the conduction band to oxygen antisites [101-103]. However, a green emission is commonly observed in ZnO prepared in oxygen-deficient environments resulting in the vacancy of oxygen, and they have attributed it to donor V_o– acceptor V_{Zn} recombination. Other possible emissions, corresponding to host ZnO phosphors, at 620 nm (2.0 eV) and 388 nm (3.19 eV), are not observed in the present case [104,105]. Recently photoluminescence studies on sol-gel derived ZnO: Gd^{3+} have been reported, and they have observed emissions in blue, green, and red regions. However, there is a difference in peak position and the nature of the photoluminescence spectra compared to reported one. The difference in PL spectra might be attributed to the difference in the excitation wavelengths and the method of synthesis [106].

Table 3: Intensity of PL peaks, energy, and wavenumbers for ZnO nanoparticles.

| T (ºC)	λ (nm)	E (eV)	I (au)	λ(nm)	E (eV)	I (au)	λ (nm)	E (eV)	I (au)
600	393	3.159	15.19	403	3.081	8.54	409	3.035	7.66
800	395	3.143	9.73	403	3.081	7.11	411	3.020	5.87
1000	395	3.159	8.99	403	3.081	6.66	411	3.020	6.64
1200	393	3.159	10.27	405	3.065	7.81	419	2.963	5.00
T (ºC)	λ (nm)	E(eV)	I (au)	λ (nm)	E(eV)	I (au)	λ (nm)	E (eV)	I (au)
600	419	2.963	6.19	443	2.802	7.92	471	2.636	2.79
800	425	2.921	7.04	445	2.790	7.47	469	2.647	2.45
1000	425	2.924	5.35	447	2.777	6.68	475	2.613	2.78
1200	429	2.894	5.40	449	2.765	4.55	477	2.603	2.49
T (ºC)	λ (nm)	E(eV)	I (au)	λ (nm)	E(eV)	I (au)			
600	483	2.570	2.76	500	2.483	3.52			
800	483	2.570	3.02	505	2.458	3.64			
1000	485	2.559	4.29	513	2.420	3.96			
1200	487	2.549	2.68	525	2.365	3.23			
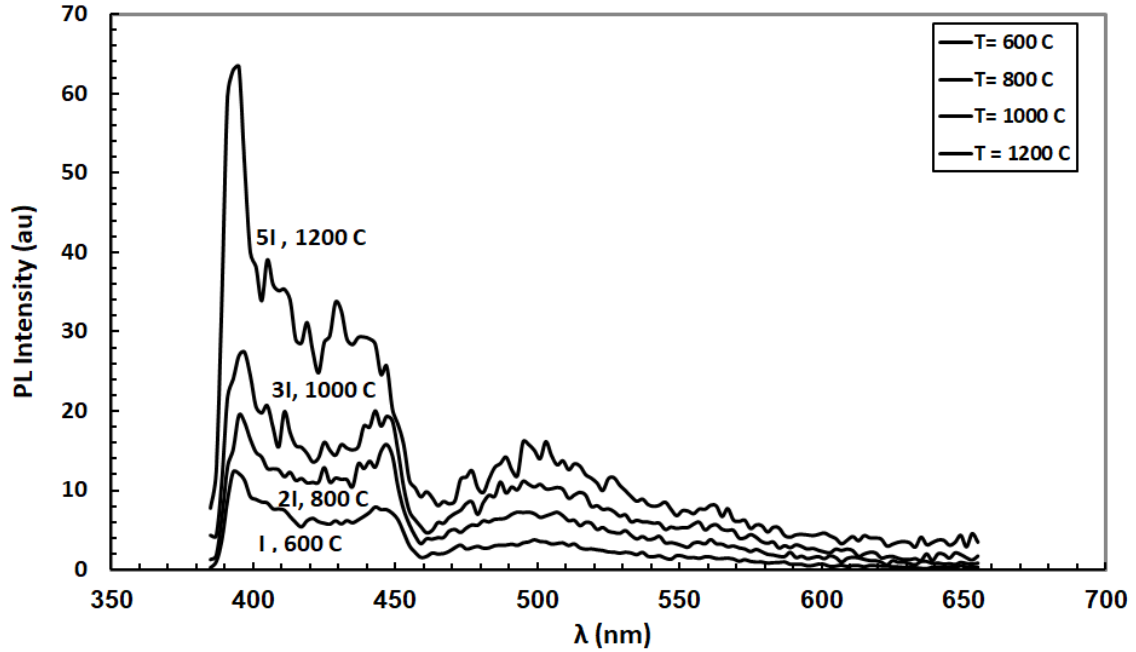
Figure 10: PL intensity versus wave number for sintered ZnO nanoparticles.

Conclusion

Structural, electrical, Photoluminescence (PL), and optical properties of ZnO nanoparticles samples are investigated. We have shown that the sintering temperature T_s does not influence the wurtzite structure of the samples, while the lattice constants and average crystallite diameters are affected. By increasing T_s up to 1200 °C, the breakdown field E_B and nonlinear coefficient β are decreased, whereas the residual voltage K_r and nonlinear conductivity σ_2 are increased. The empirical relations indicated that E_B would be zero for ZnO at T_s= 1433.09 °C. As the T_s increases up to 1200 °C, a maximum UV shift for absorption (A_{max}) occurs at 412, 400, 384, and 326 nm, respectively. Two different values of the band gap are obtained for each sample; the first is the fundamental energy gap (E_{gh}) and its value above 3 eV, while the second is the optical energy gap (E_{gL}) and its value below 2.1 eV. Moreover, E_{gh} will be zero for ZnO at T_s = 120°C. The values of (N/m^*) and ε_L for the samples are increased as T_s increases up to 1200 °C. The vice is versa for inter-atomic distance R. The dielectric loss tanδ is almost linear above 4 eV for the samples, and it decreases sharply as the T_s increases. The optical and electrical conductivities σ_{opt} and σ_{ele} are gradually decreased as the T_s increases up to 1200 °C. The characteristic of UV band edges emission against the optimum value of PL intensity for the samples shows 8-continuous peaks. Furthermore, the PL intensity of the considered peaks is decreased by increasing T_s and by shifting the UV wave number towards the IR region.

Acknowledgments

References

1- G. D. Mahan, L.M. Levinson, H.R. Philipp, J. Appl. Phys. 50, 2799 (1979).

2- L.K.J. Vanadamme and J.C. Brugman, J. Appl. Phys. 51, 4240 (1980).

3- M. Matsuoka, T. Masuyama and Y. Iida, Suppl. J. Jpn Soc. Appl. Phys. 39, 94 (1970).

4- K. Hagemark, J. Solid State Chem., 16, 293 (1976).

5- E.A. Secco and W.J. Moore, J. Chem. Phys. 26, 942 (1957).

6- F.A. Kröger, The Chemistry of Imperfect Crystals, North- Holland, Amsterdam 2, 743 (1974).

7- G.D. Mahan, J. Appl. Phys. 54, 3825 (1983).

8- A.Sedky, M.Abu-Abdeen and Abdul-Aziz A. Almulhem, Physica B 388, 266 (2007).

9- H. Klug and L. Alexander, X-ray Diffraction Procedures, Wiley, New York, p.125 (1962).

10- J. Han, A.M.R. Senos, P.Q. Mantas, Mater. Chem. Phys. 75, 117 (2002).

11- J.M. Madou and R. S. Morrison, Chemical Sensing with Solid State Devices, Academic Press, San Diego, CA, Chapters 2,3 and 12 (1989).

12- P. Bonasewicz, W. hirscawald and G. Newnann, Phys. Stat. Sol. (a) 97, 593 (1986).

13- M.S. Castro and C.M. Aldao, J. Eur. Ceram. Soc. 19, 511 (1998).

14- H.M. Zeyada, M.M. EL-Nahass, I.S. El-Ashmawi and A.A. Habashi, , J. Non-Cryst. Solids 358, 625e636 (2012).

15- Neelam Kumari, Samya Naqvi and Rachana Kumar, J. Mater. Sci. 53, 4046e4055 (2018).

16- Nursaadah Ahmad POAD, Siti Zulaikha Ngah Demon, Muhd Zuazhan Yahya and Noriah Bidin, Int. J. Curr. Sci. Eng. Technol. 20,1262e268 (2018).

17- M.H. Shahrokh Abadi, A. Delbari, Z. Fakoor and J. Baedi, J. Ceram. Sci. Technol. 6 , 41e46 (2015).

18-M. S. Ramanachalam, A. Rohatgi, W. B. Carter, J. P. Schaffer and T. K. Gupta, Journal of Electronic Materials 24, 4, 413 (1995).

19- B.L. Zhu, X.H. Sun, X.Z. Zhao, F.H. Su, G.H. Li and X.G. Wu,Vacuum 82, 495 (2008).

20- S.J. Kang, Y.H. Joung, H.H. Shin and Y.S. Yoon, J. Mater. Sci.: Mater. Electron. 19, 1073 (2008).

21- F.K. Shan, Z.F. Liu, G.X. Liu, W.J. Lee, G.H. Lee and I.S. Kim, J. Electroceram. 13, 195 (2004).

22- H.S. Kang, J.S. Kang, S.S. Pang, E.S. Shim and S.Y. Lee, Mater. Sci. Eng. B 102, 313 (2003).

23- V.R. Shinde, T.P. Gujar, C.D. Lokhanade, R.S. Mane and S.H. Han, Mater. Chem. Phys. 96, 326 (2006).

24- K. Eda, A. Ega and M. Matsuoka,J. Appl. Phys. 51, 2678 (1980).

25- K. Sato, Y. Takada, H. Makewa, M. Ototake and S. Tominga, Jpn. J. Appl. Phys. 19, 909 (1980).

26-T.K. Gupta, W.G. Carlson and P.L. Hower, J. Appl. Phys. 52, 4104 (1981).

27- R. Einzinger,Grain Boundaries in Semiconductors, ed. H.J. Leamy, G.E. Pike and C.H. Seager (New York: Elsevier), p. 343 (1982).

28- T.K. Gupta and A.C. Miller,J. Mater. Res. 3, 4, 745 (1988).

29- Q. Shen, T. Toyoda, Jpn. J. Appl. Phys. 39, 511 (2000).

30- Q. Shen, T. Toyoda, Jpn. J. Appl. Phys. 39, 3146 (2000).

31- S. Abdalla, K. Easawi**,** T. A. El-Brolossy, G. M. Yossef, S. Negm and H. Talaat, Rev. Sci. Instrum., 74 No (1), 848 (2003).

32- T. A. El-Brolossy, S. Abdalla, O. E. Hassanein, S. Negm, and H. Talaat, J. Phys IV France, 125. 685 (2005).

33- K.S. Shankar, S. Kar, G. N. Subbanna and A .K .Raychaudhuri, Sol. State. Comm. 129, 479, (2004).

34- A. Dutta, N. Gayathri and R. Ranganathan, Phys. Rev. B 68, 054432 (2003).

35- G. Venkataiah et al Physica B 357, 377, (2005).

36- M. A. Lopez-Quintela, L. E. Hueso, J. Rivas and F. Rivadulla.Nanotechnology 14, 212 (2003).

37- H. Ohno, Science. 281 951 (1998).

38- A.Sedky, S. A Amin and Mohamed M, Applied Physics A 125 308 (2019).

39- S.A. Amin and A.Sedky, Mater. Res. Express 6, 065903 (2019).

40- Choon – Woo Nahm and Byoung – Chil Shin, Mater. Lett. 57, 1322 (2003).

41- M.S. Castro, C.M. Aldao, J. Eur. Ceram. Soc. 19, 511 (1998).

42- G. Pei, C. Xia, S. Cao, J. Zhang, F. Wu, J. Xu, J. Magn. Mater.302 (2), 340 (2006).

43- C.H. Bates, W. B. White, Science 137, 993 (1962).

44- Guangqing Pei, Changtai Xia, Shixun Cao, Jungang Zhang, Feng Wu and Jun Xu, JMMM 302, 2, 340 (2006).

45- A.Sedky, Brazilian J physics 44, 4, 305 (2014).

46- Kisi E , Elcombe M M, Acta Crystallogr., Sect. C: Cryst. Struct.Commun.C 45, 1867 (1989).

47- Özgür Ü , Ya A, Alivov I, Liu C, Teke A, Reshchikov M A, Doğan S, Avrutin C V, Cho S J and Morkoçd, J. Appl. Phys. 98, 041301 (2005).

48- A. Sedky and S. B. Mohamed, Materials Science-Poland, 32(1), 16 (2014).

49- T.Hanad, http://www.Springer.com/978-3-540-88846-8(2009).

50- S. Aksoy, Y. Caglar, S. Ilican, M. Caglar and Chem. Eng. Civ. Eng. Mech. Eng. 227, (2010).

51- U. Seetawan, S. Jugsujinda, T. Seetawan, A. Ratchasin, C. Euvananont, C. Junin, C. Thanachayanont, P. Chainaronk, Mater. Sci. Appl. 2 , 1302 (2011).

52- E. Muchuweni, T.S. Sathiaraj and H. Nyakotyo, Heliyon 3 , e00285, 1(2017).

53- A.Sedky, Advances in Material Sci. Eng. 2,1 ,1(2018).

54- F.K. Shan, Z.F. Liu, G.X. Liu, W.J. Lee, G.H. Lee and I.S. Kim, J. Electroceram. 13, 195 (2004).

55- S. A.Amin and A.Sedky, Mater.Res.Express 6, 065903, (2019).

56- X.S. Wang, Z.C. Wu, J.F. Webb, Z.G. Liu, Appl. Phys. A 77, 561 (2003).

57- Xuhai Li, Xiuxia Cao, Liang Xu, Lixin Liu, Yuan Wang, Chuanmin Meng and ZhigangWang, J. Alloys & Compounds 675, 90 (2016).

58- A.Sedky, M.Abu-Abdeen and Abdul-Aziz A. Almulhem, Physica B 388, 266 (2007).

59- A.Sedky, T. A El- Trabolosy and S.B.Mohamed, J. of Physics and Chemistry of Solids 73, 505 (2012).

60- A.Sedky and E.El-Suheel, Physics Research International 2010, 1 (2010).

61- T.K. Gupta, J. Am. Cream. Soc. 37 (7), 1817 (1990).

62- Wan Rafizah Wan Abdullah, Azmi Zakaria and Mohd Sabri Mohd Ghazali, Int. J. Mol. Sci. 13, 5278 (2012).

63- Shengtao Li, Feng Xie, Fuyi Liu, Jianying Li, Mohammad A. Alim, Materials Letters 59, 302 (2005).

64- A. Sedky, International J of Photonics and Optical Technology 3, 3 ,1(2017).

65- J. W. Fergus, J. Mater. Sci. 38, 4259 (2003).

66- H. M. Ali and A. M. Abdel Hakeem, Phys. Status Solidi A 207, 1, 132 (2010).

67- E.R. Shaaban, M.M. Soraya, M. Shapaan, H. Shokry Hassan and M.M. Samar, J. Alloy. Compd. 693, 1052 (2017).

68- Q. Shen and T. Toyoda, Jpn. J. Appl. Phys., 39, 3146 (2000).

69- S. Abdalla, K. Easawi, T.A. El-Brolossy, G.M. Yossef, S. Negm and H. Talaat, Rev. Sci. Instrum. 74, 1, 848 (2003).

70- A.A. Othman, M.A.Othman, E.M.M. Ibrahim and Manar.A.Ali, Ceramic International 43, 527 (2017).

71- H. M. Ali, H. A. Mohamed, and S. H. Mohamed, Eur. Phys. J. Appl. Phys. 31, 87 (2005).

72- S.J. Darzi and A.R. Mahjoub and A. Nilehi, Phys. E Low-Dimens. Syst. Nanostructures 42, 1, 76 (2009).

73- A. El-Denglawey, Journal of Luminescence 194, 381 (2018).

74- J. Yu, X. Zhao and Q. Zhao, Mater. Chem. Phys. 69,25 (2001).

75- Suresh Sagadevan, Kaushik Pal, Zaira Zaman Chowdhury and M. Enamul Hoque, Journal of Sol-Gel Science and Technology volume 83, pages394-404(2017)

76-Raid A. Ismail , Abdulrahman K. Ali , Mukhlis M. Ismail and Khaleel I. Hassoon, Appl Nanosci (2011) 1:45-49.

77- Y.G. Wang, S.P. Lau, H.W. Lee, S.F. Yu, S.K. Tay, X.Z. Zang and H.H. Hing, J. Appl. Phys. 94, 354 (2003).

78- H. Abdel-Khalek, E. Shalaan , Mohamed Abd- El Salam, Aida M. El-Sagheer and Ahmed M. El-Mahalawy, Journal of Molecular Structure 1178, 408 (2019).

79- H.M. Zeyada, M.M. EL-Nahass, I.S. El-Ashmawi and A.A. Habashi, Current Applied Physics 13, 9, 1960 (2013).

80. L.M. Su, N. Grote and F. Schmitt, Electron. Lett. 20, 717 (1984).

81- T.K. Kundu, N. K., P. Barik and S. Saha, Int. J. Soft Comput. Eng. (IJSCE). ISSN: 2231-2307, volume 1, issue NCRAMT2011 (2011).

82- C.P. Lin, H. Chen, A. Nakaruk, P. Koshy and C.C. Sorrell, Energ Pro. 34,627 (2013).

83- Hazem Mahmoud Ali and Ahmed Mohamed Abdel Hakeem, Eur. Phys. J. Appl. Phys.72,10301 (2015).

84- E. Burstein, Phys. Rev. 93, 632 (1954).

85-A. El-Denglawey, Non-Cryst. Solids 357,1757 (2011).

86- A.A. Zaki and A.A. El-Amin, Optics and Laser Technology 97, 71 (2017).

87- Hazem Mahmoud Ali and Ahmed Mohamed Abdel Hakeem, Eur. Phys. J. Appl. Phys. 72,10301(2015).

88- 75- M.S. El-Bana and S.S. Fouad, J.Alloys and Compd. 695,1532 (2017).

89- M. M. El-Desoky, J. Non-Cryst. Solids 35, 139 (2005).

90- Fouad, M.S. El-Bana, Pankaj Sharma and Vineet Sharma, J.Alloys and Compd. 667,204 (2016).

91- Y.Li,L.Xu, Li.X. Shena and A.Wang, Appl. Surf. Sci. 256, 45439 (2010).

92- M. Dongol, M.M. El-Nahass, M. Abou-Zied and A. El-Denglawey, Eur.Phys. J. Appl. Phys. 37, 257 (2007).

93- M. Dongol, M.M. El-Nahass, M. Abou-Zied and A. El-Denglawey, Physica B 371, 218 (2006).

94- K.Ali and Farid M. Abdel-Rahim, J.Alloys and Compd. 561,284 (2013).

95- T. Girisun and S. Dhanuskodi, Crys. Res. Technol. 44, 1297 (2009).

96- S.S. Fouad, I.M. El-Radaf, Pankaj Sharma, J.Alloys and Compd. 757,124 (2018).

97- Y. S. Wang, P. John Thomas, and P. O'Brien, J. Phys. Chem. B, 2006, 110 (43), 21412 (2006).

98- K. Vanheusden, W.L. Warren, C.H. Seager, D.R. Tallant, J.A. Voigt and B.E. Gnade,J. Appl. Phys., 79, 7983–7985 (1996).

99- X.M. Fan, J.S. Lian, L. Zhao and Y. Liu, Appl. Surf. Sci., 252, 420–424 (2005).

100- T. Tatsumi, M. Fujita, N. Kawamoto, M. Sasajima and Y. Horikoshi, Jpn. J. Appl.Phys., 43, 2602–2606 (2004).

101- Y.W. Heo, D.P. Norton and S.J. Pearton, J. Appl. Phys., 98, 073502 (2005).

102- T.E. Murphy, K. Moazzami and J.D. Phillips, J. Electron. Mater., 35, 543–549(2006).

103- B. Lin, Z. Fu and Y. Jia, Appl. Phys. Lett., 79, 943–945 (2001).

104- K. Potzger, S. Zhou, F. Eichhorn, M. Helm, W. Skorupa, A. Mcklich, J. Jassbender,T. Herrmannsdorfer and A. Bianchi, Appl. Phys. Lett., 99, (1–5) 063906 (2006).

105- Suman Rani, Bansi Lal, Sumit Saxena and Shobha Shukla, J. Sol–Gel Sci. Tech.,81, 586–592 (2017).

106- G. Krishna Reddy, A. Jagannatha Reddy, R. Hari Krishna, B.M. Nagabhushana, G. Ram Gopal, Journal of Asian Ceramic Societies 5 (2017) 350–356

Figures
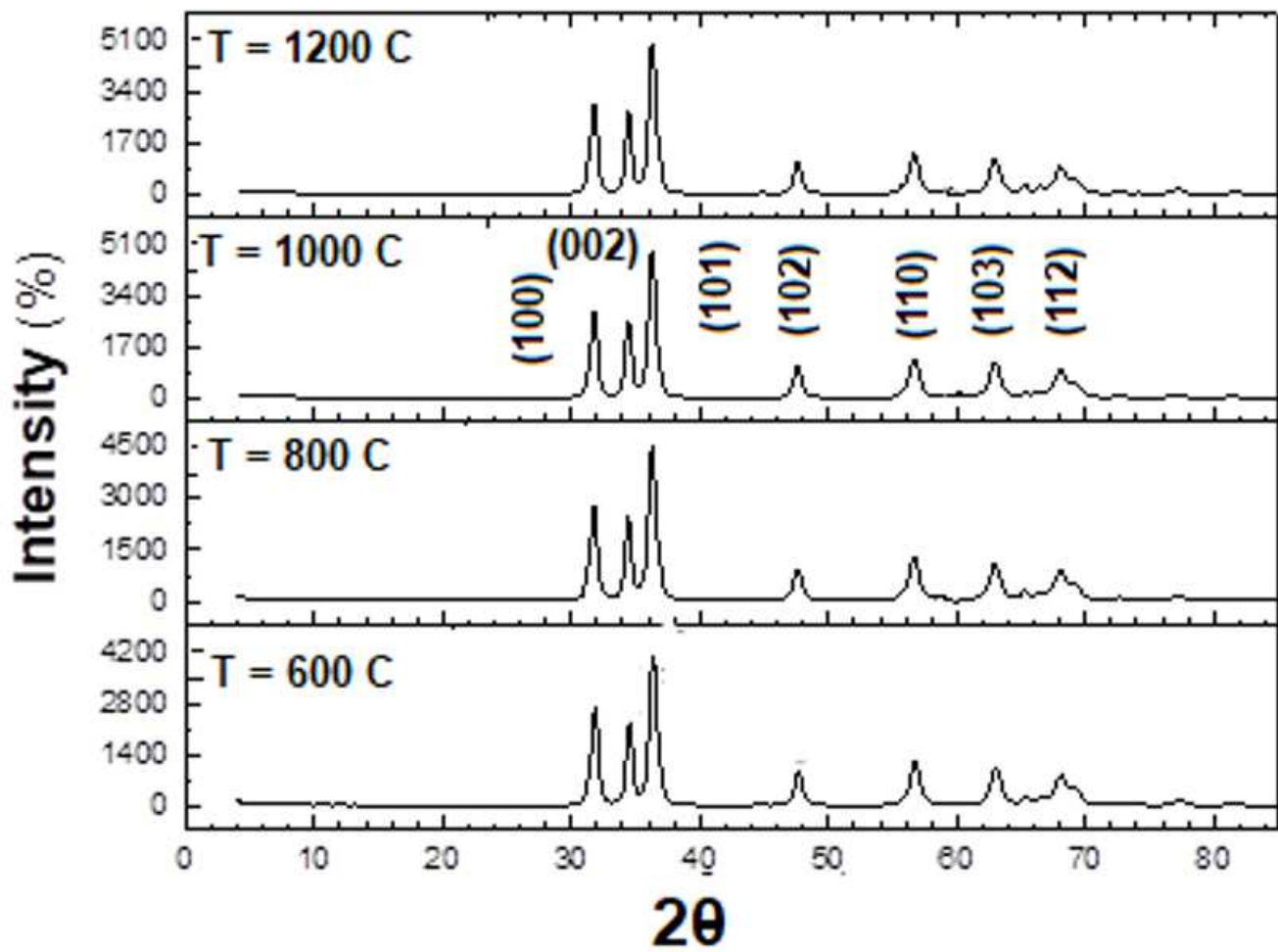
Figure 1

X-ray diffraction pattern for ZnO nanoparticles.

T = 600 ºC

T = 800 ºC

T = 1000 ºC

T = 1200 ºC
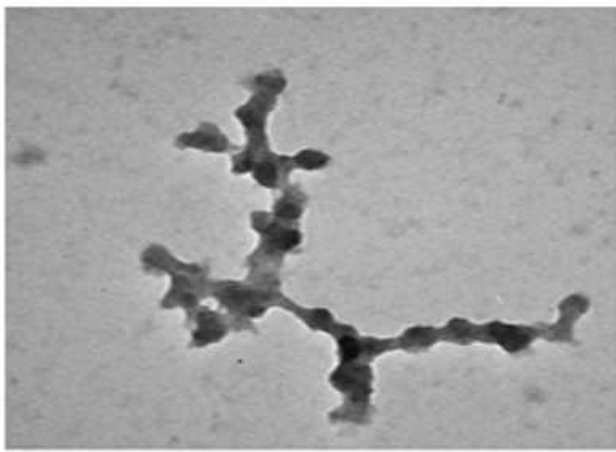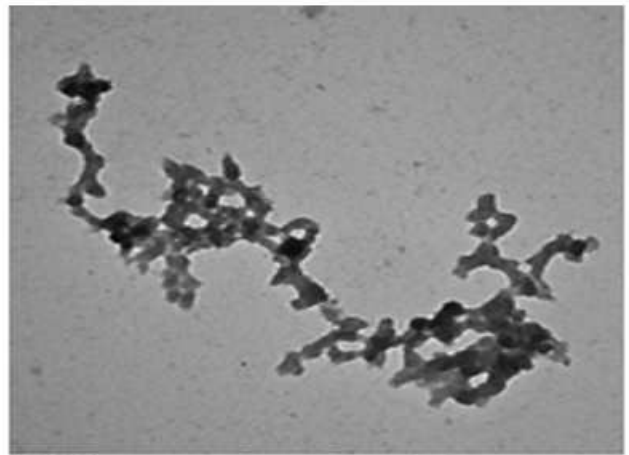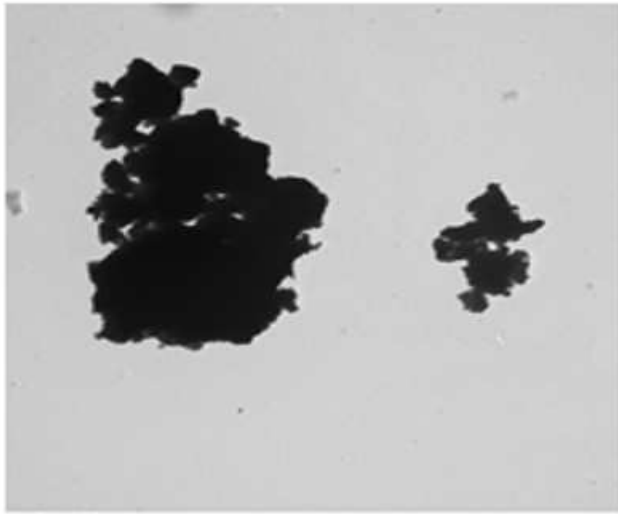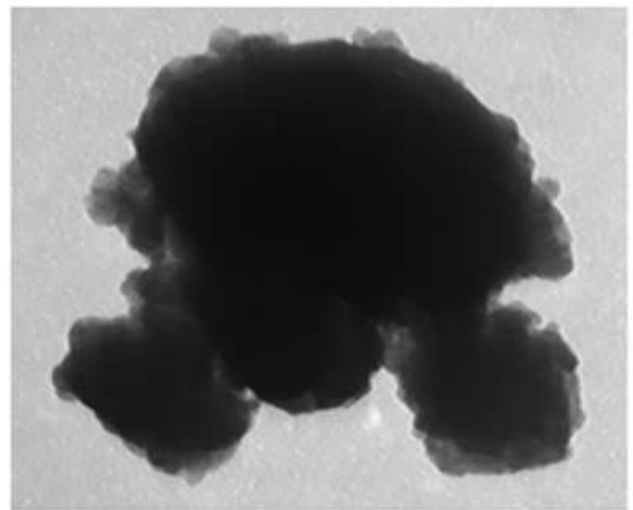
Figure 2

TEM images for ZnO nanoparticles.
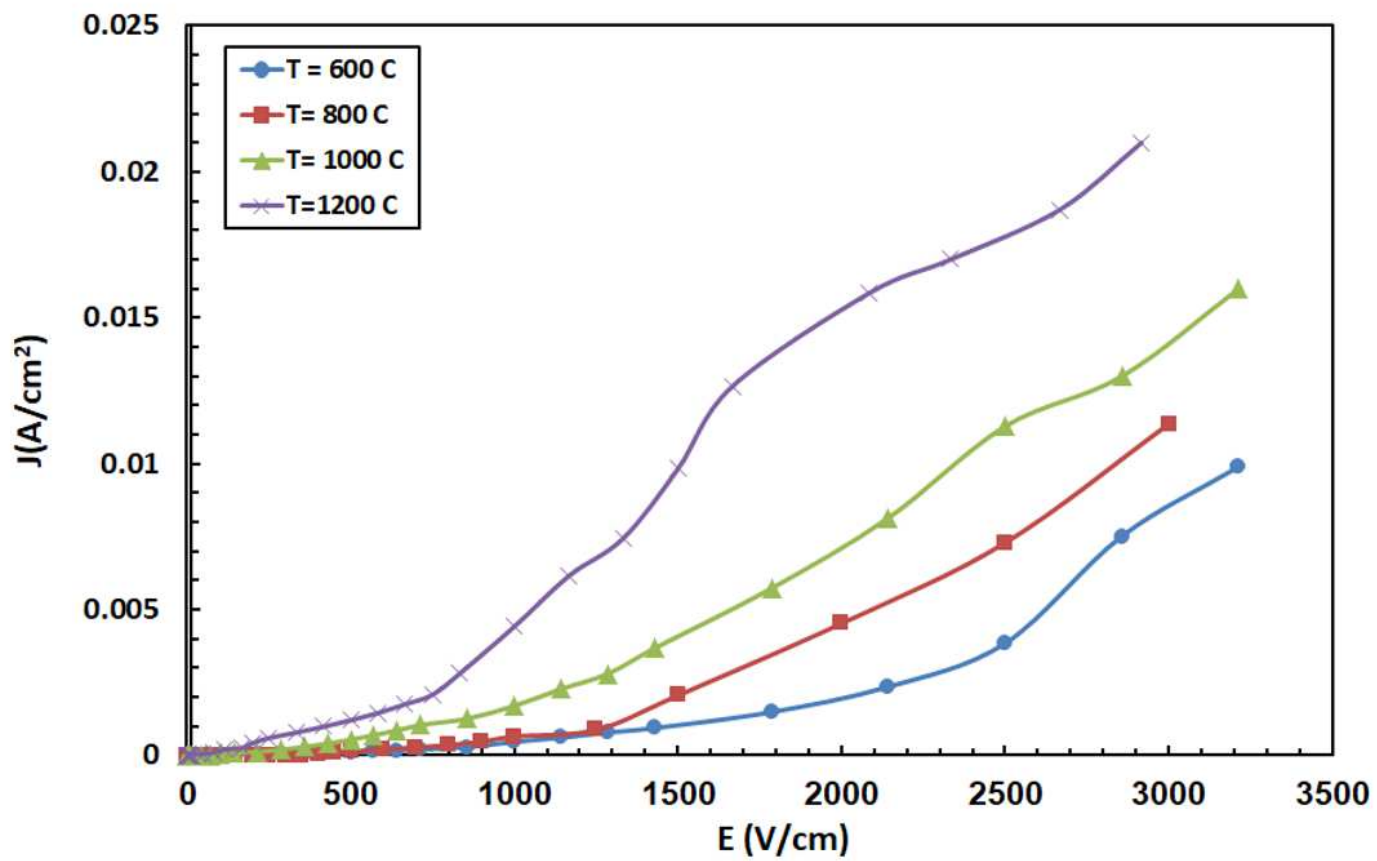
Figure 3

J-E curves versus Ts for ZnO nanoparticles.
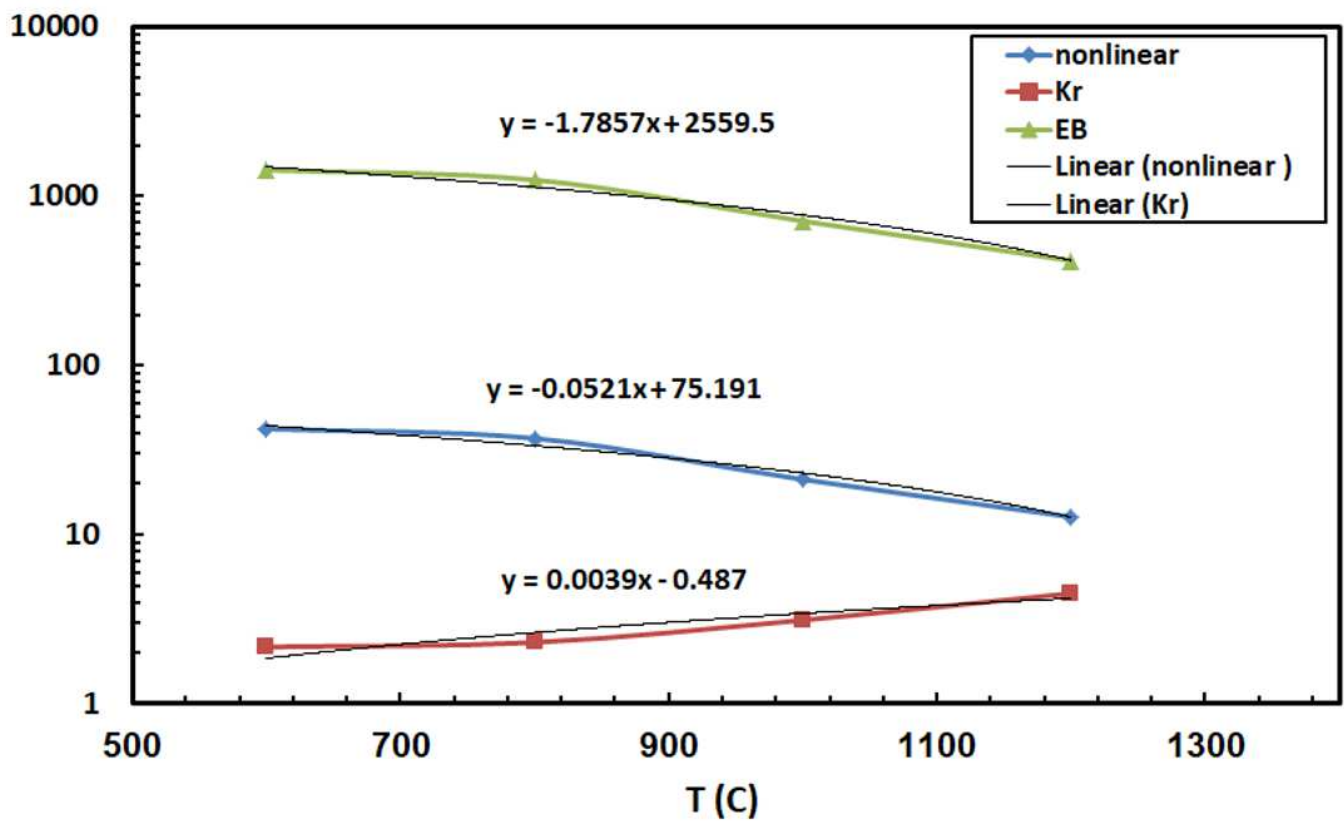
**Figure 4**

EB, β and Kr versus Ts of ZnO nanoparticles.
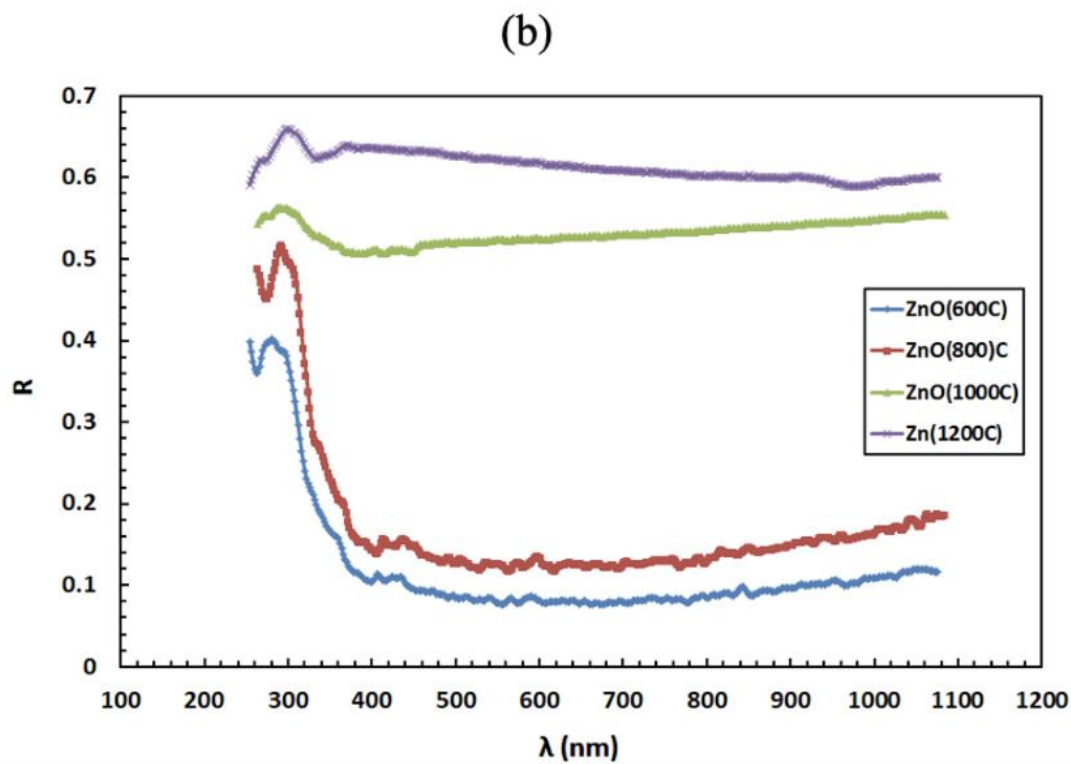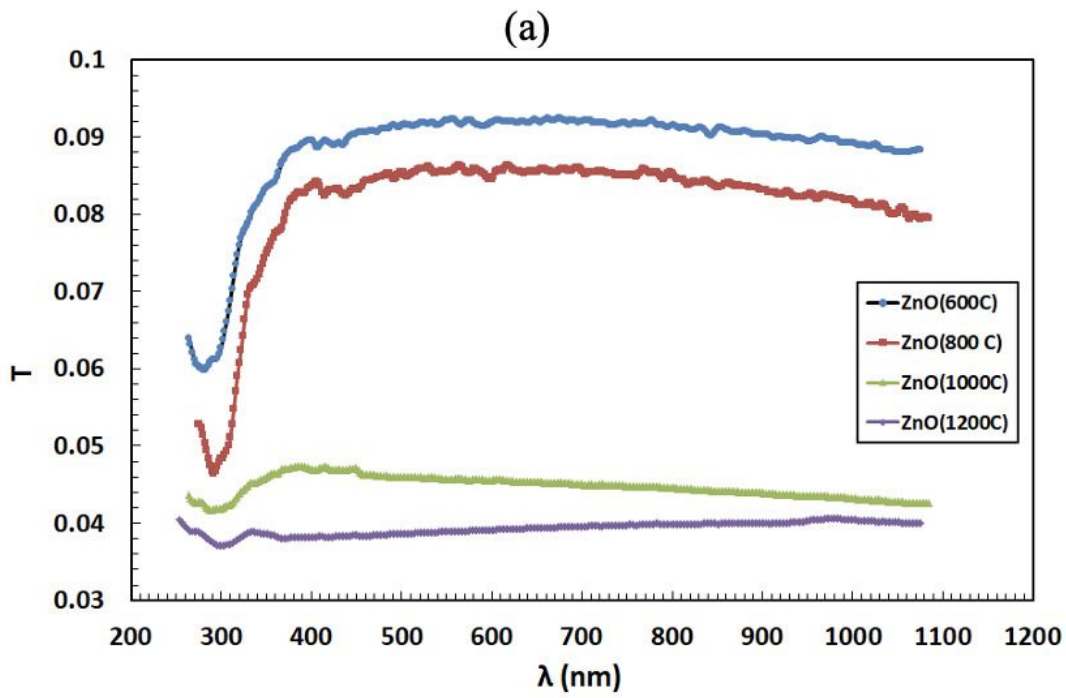
Figure 5

(a): Transmittance versus wave length for ZnO nanoparticles. (b): Reflectance versus wave length for ZnO nanoparticles
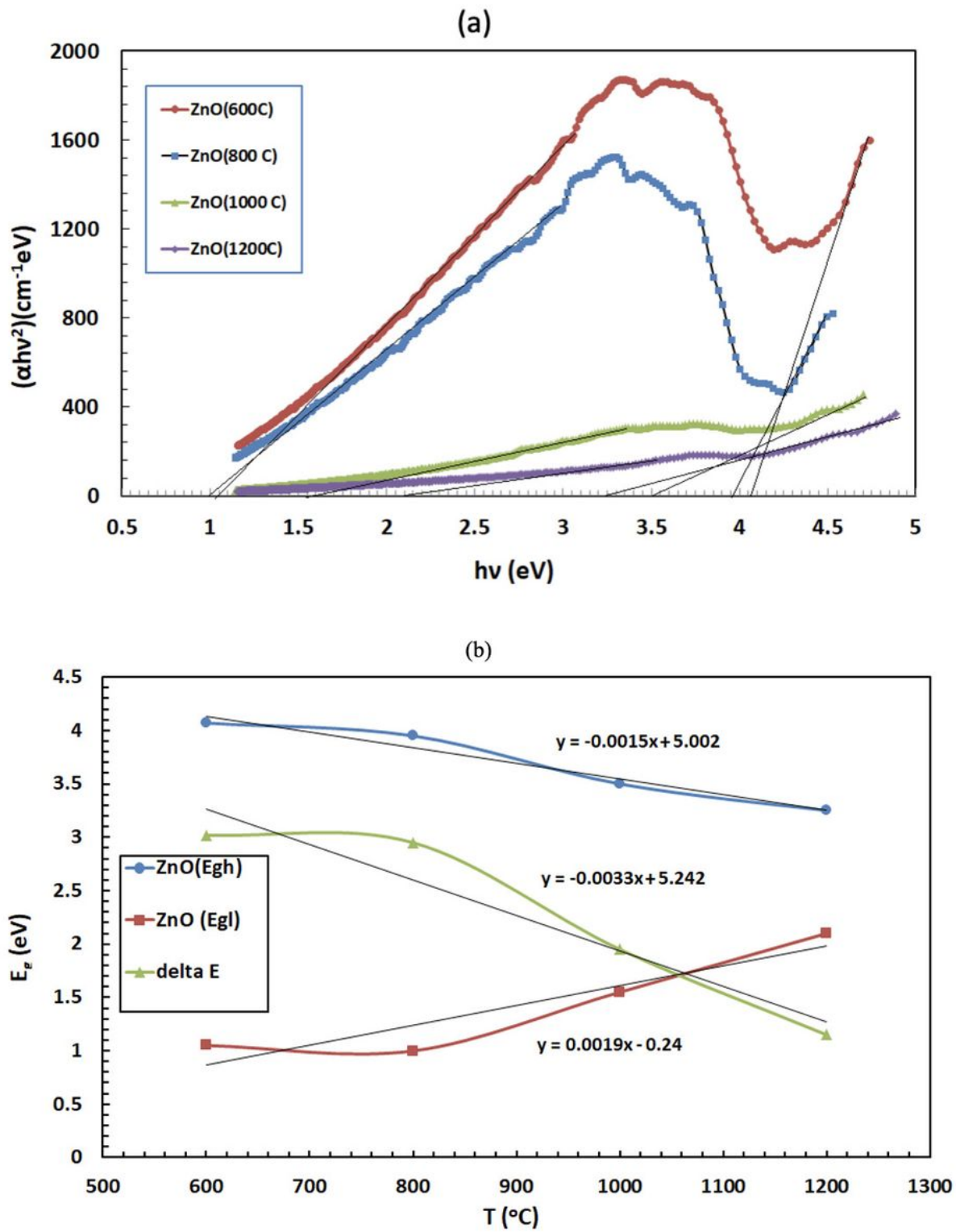
Figure 6

(a): (αhν)2 versus photon energy for sintered ZnO nanoparticles. (b): Eg versus Ts for ZnO nanoparticles.
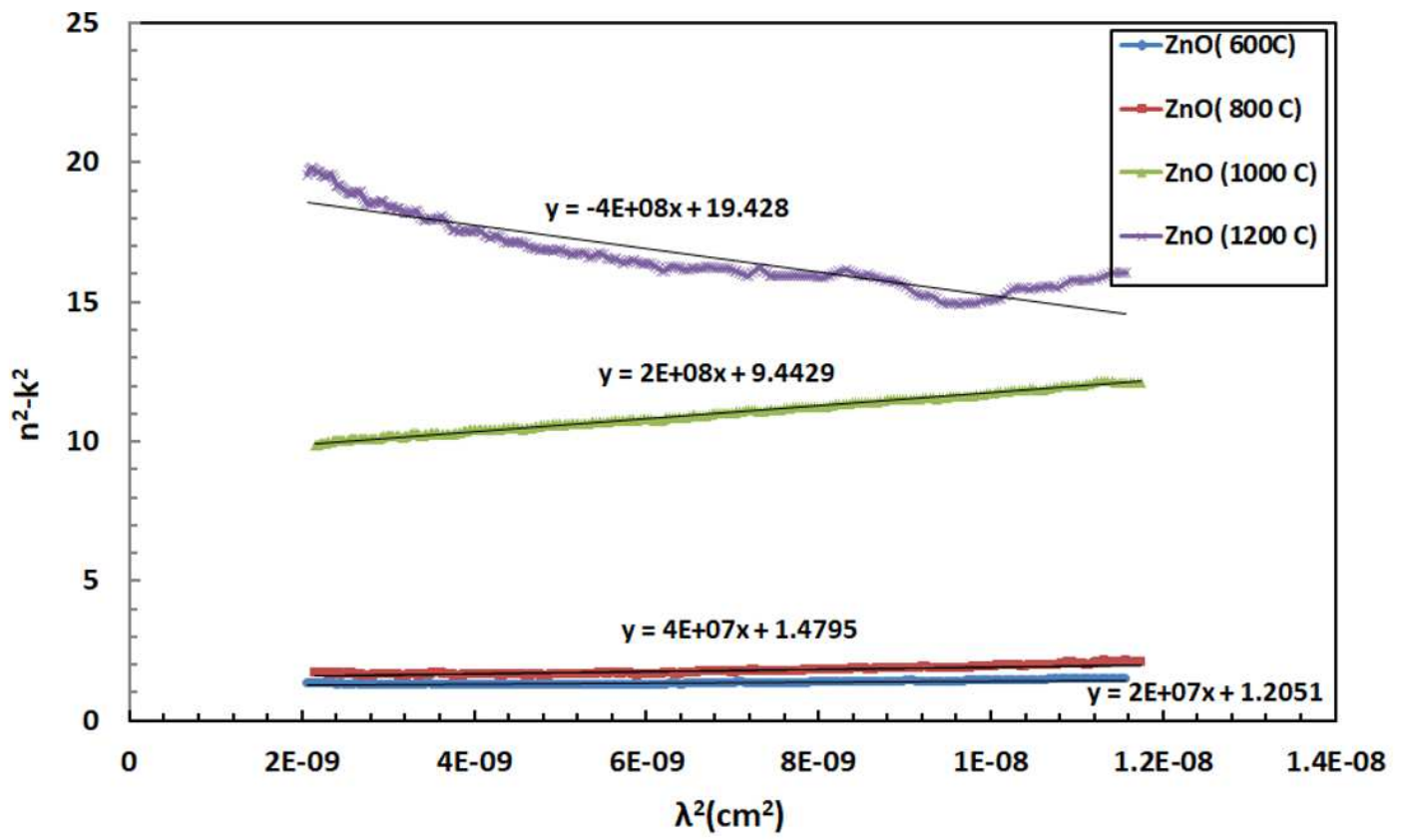
Figure 7

The relation between (n2-k2) and λ2 for ZnO nanoparticles.
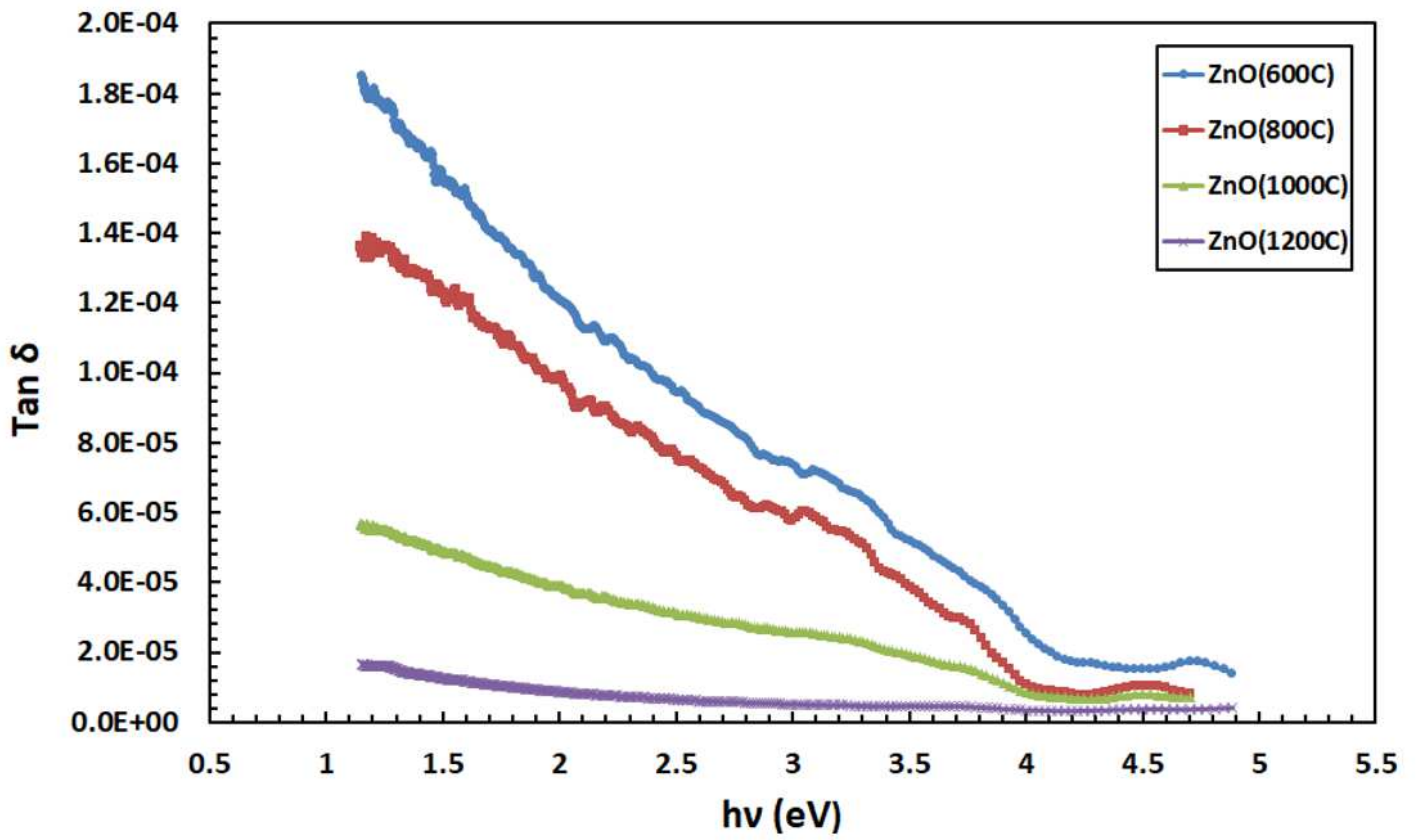
Figure 8

Dielectric loss versus hv for ZnO nanoparticles.

(a)

(b)
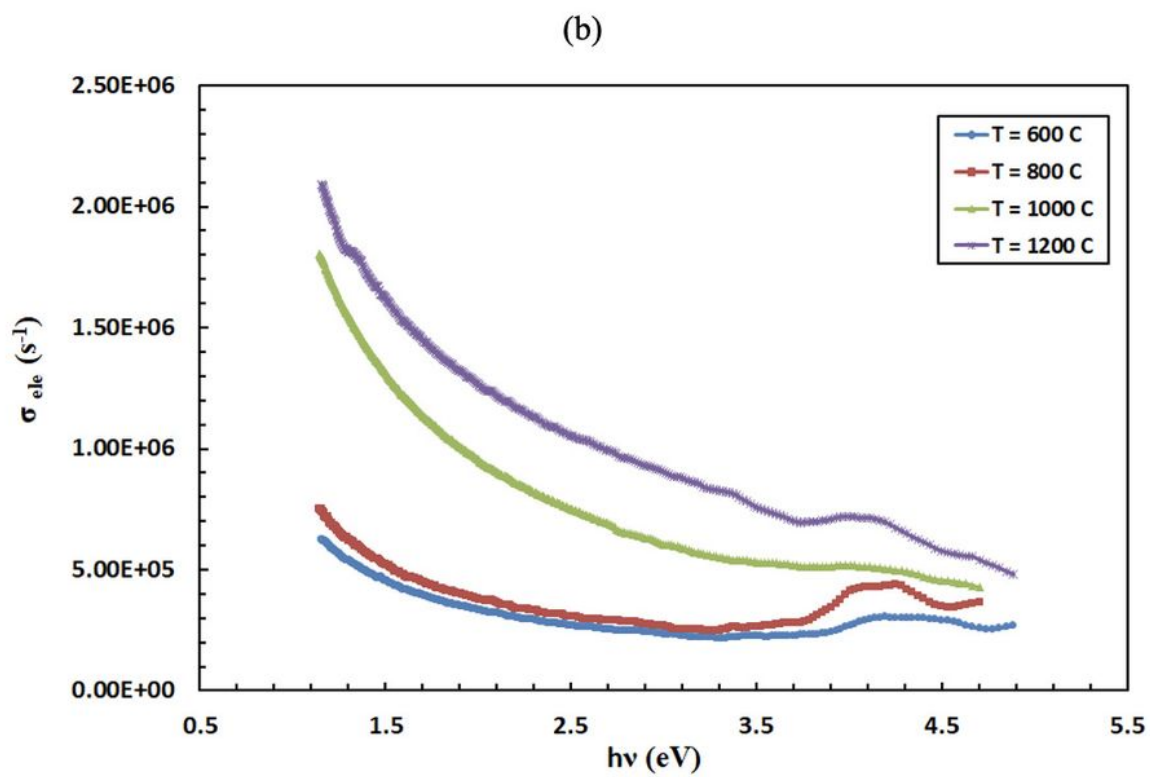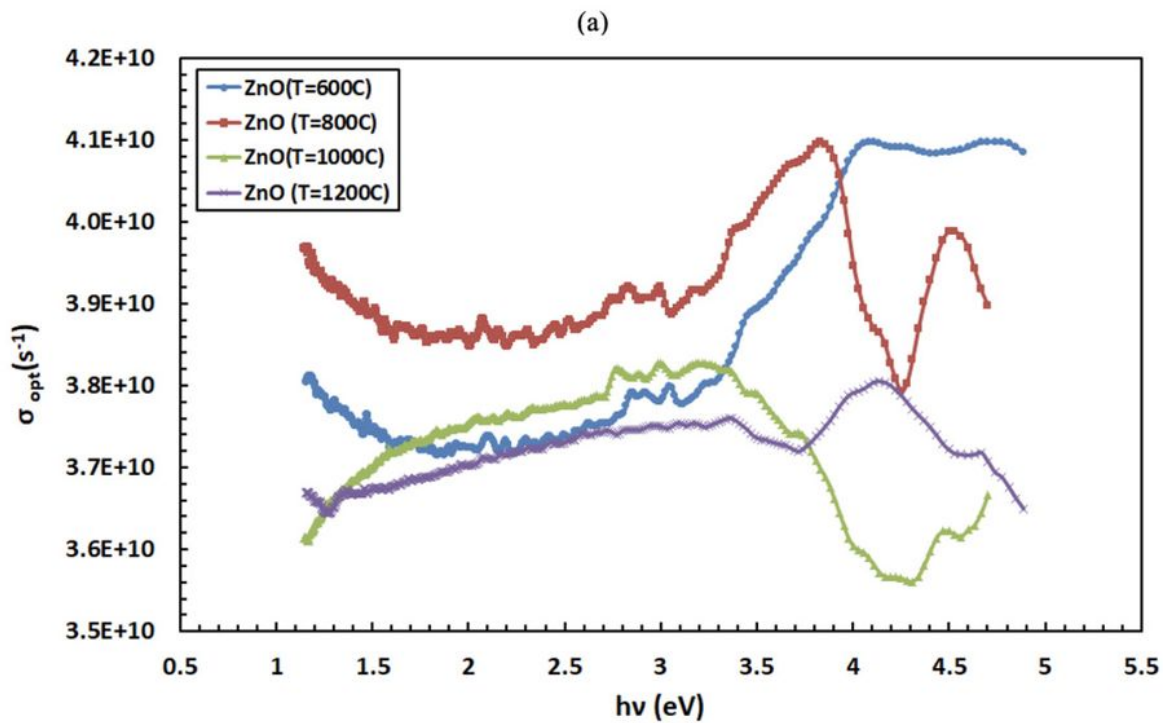
Figure 9

(a): Optical conductivity versus hv for ZnO nanoparticles. (b): Electrical conductivity versus hv for sintered ZnO nanoparticles.

Figure 10

PL intensity versus wave number for sintered ZnO nanoparticles.